Vilnius University
Faculty of Physics
Laser Research Center

Dharma Prasetya Permana

Propagation of Optical Vector Vortices in Coherently Prepared Media

Master's Thesis

Laser Physics and Optical Technologies study program

Student	Dharma Prasetya Permana
Approved	2026 - 05 - 22
Academic Supervisor	Dr. Hamid R. Hamedi
Consultant	Dr. Mažena Mackoit Sinkevičienė
Reviewer	Dr. Artūras Acus
Director of Laser Research Center	Dr. Dalia Kaškelytė

Vilnius 2026

Contents

List of Abbreviations

- **BG** . . . . Bessel-Gaussian
- **CV** . . . . Cylindrical vector
- **EIT** . . . . Electromagnetically induced transparency
- **HG** . . . . Hermite-Gaussian
- **LC-SLM** . . . . Liquid-crystal spatial modulator
- **LG** . . . . Laguerre-Gaussian
- **LVNE** . . . . Liouville-Von Neumann Equation
- **MBE** . . . . Maxwell-Bloch Equation
- **OAM** . . . . Orbital angular momentum
- **RWA** . . . . Rotating wave approximation
- **SAM** . . . . Spin angular momentum
- **SOP** . . . . State of polarization
- **SPP** . . . . Spiral phase plate
- **SVEA** . . . . Slowly varying envelope approximation
- **TDSE** . . . . Time-dependent Schrödinger equation
- **VV** . . . . Vectorial vector

Introduction

Over the past decades since its introduction by Coullet et al. [1], optical vortices have attracted increasing interest, particularly due to their promising applications in high-dimensional quantum communication and information processing [2–5]. An optical vortex is a special type of light beam that carries orbital angular momentum (OAM) with a discrete value of $l\hbar$, where l can take any integer value without bound [6]. The integer l is directly related to the topological charge of the phase singularity, which corresponds to the helical phase factor $e^{il\phi}$, where ϕ is the azimuthal coordinate in the plane transverse to the propagation direction [7]. Moreover, the potential for high-dimensional quantum information processing offered by optical vortices can be further enhanced by combining OAM states with the spin angular momentum (SAM) states of light, which are associated with the beam's polarization [8].

To manipulates vortex as the tool for quantum information processing, it is important to study its interaction with matter. A particularly interesting case of light-matter interaction happens within the medium consisting of atomic ensembles that lead to the discovery of electromagnetically induced transparency (EIT) [9–11]. When an optical vortex interacts with EIT-enabled atomic medium, a range of novel phenomena emerge such as the transfer of OAM of light [12, 13], azimuthally dependent transparency [14], and entanglement of OAM states in photon-pairs [15]. However, most of these demonstrated phenomena have focused only on the cases involving scalar vortex where the polarization state is uniform across the beam cross-section, thus, leaving the SAM properties of the vortex beam unexplored.

To enable the utilization of SAM in optical vortices, the full vectorial aspect of vortex beam must be considered, which leads to the notion of vector vortex beam. A vector vortex beam is composed of a superposition of two vortex beams with orthogonal polarizations, resulting in a spatially varying polarization distribution [16–20]. The interaction of such beams with EIT-enabled atomic media has been explored and has led to several intriguing phenomena. Among them are spatially dependent transparency [21,22] in a four-level tripod atomic system, which can be utilized as an atomic compass [23], and transfer of SAMs [24]. However, these type of EIT systems rely on the presence of weak transverse magnetic field to establish a closed loop among the atomic states and facilitate a coherent superposition, thus, limiting their application where a weak magnetic field is present.

In our previous work, we investigated the interaction of vectorial vortex beams with EIT-enabled atomic systems in a coherently prepared three-level Λ configuration without an external magnetic field [25]. We showed that the spin-orbit interaction of light can arise in this system, leading to spatially dependent transparency and SAM exchange. However, the slow-light propagation regime of vector vortices was not explored in that study. This regime refers to a condition in which the propagation speed of a weak optical pulse is dramatically reduced in an EIT-enabled atomic medium through the presence of a stronger control field [26–28]. It is particularly interesting because several phenomena associated with slow light, including enhanced optical nonlinearities [29–31], light storage [10, 32], and stationary light [33–35], can be combined with the spin-orbit interaction of light. Such a combination may offer promising opportunities for storing quantum information encoded in structured light within an atomic medium. Another important limitation of our previous investigation in the coherently prepared Λ configuration without a strong control field is that, although spatially dependent transparency emerges from the weak interaction between vector vortices and the EIT medium, the beam still undergoes strong absorption in the azimuthally non-transparent regions upon entering the medium. This leads to a rapid transformation of both the beam intensity and polarization state over a short propagation distance, which in turn reducing the precision to the control the spin-orbit properties of light.

The goal of this study is to investigate the interaction of vectorial vortex beams with coherently prepared EIT-enabled atomic systems in the presence of a strong control field. In particular, we demonstrate that spatially dependent transparency and SAM exchange can occur in the slow-light propagation regime, and show that the control field provides an effective means to tune the dynamics of the spin-orbit interaction of light.

The tasks set to achieve this goal are as follows:

1. Use the Liouville-Von Neumann equation to derive the Bloch equations describing the population dynamics of a coherently prepared atomic system in the presence of a strong control field.

2. Find the solutions for the atomic coherences from the Bloch equations in the steady-state and weak-probe limits.

3. Solve the Maxwell–Bloch propagation equations for vortex pairs in the linear regime.

4. Study the influence of the strong control field on the absorption, dispersion, group-velocity reduction, and polarization dynamics using the obtained coherences and the solutions of the Maxwell–Bloch equations.

1 Literature review

1.1 Atom-light interaction: two-level system

As the core of this work is to study the interaction of light and matter, we will start by considering the simplest model of interaction between single mode electromagnetic fields, with a two-level atomic system. Although simple, this model of interaction is crucial and will be our main building blocks for investigating an interaction scheme with higher complexity that will be discussed throughout this work. Moreover, we restrict our work in the semi-classical framework. In this framework, the atomic system is treated quantum mechanically, while the electromagnetic-field-driven interaction is treated classically.

1.1.1 Hamiltonian of the atom-field system

Consider a two-level atomic system with a ground state $|g\rangle$ and an excited state $|e\rangle$ called the atomic bare states. The bare states themselves are the eigen-states of the unperturbed atomic Hamiltonian $\hat{H}_0$ with the eigen-values (energies) $\hbar\omega_g$ and $\hbar\omega_e$ for $|g\rangle$ and $|e\rangle$ respectively, where $\hbar = 1,054\times10^{-34}$ J·s is the reduced Planck constant. When this atom is illuminated by a monochromatic laser field with frequency ω, a transition between the two levels is driven as depicted in Fig. 1. The wave-function of this system can be written as a combination of the atomic bare states:

$$|\psi(t)\rangle = C_g(t)\,|g\rangle + C_e(t)\,|e\rangle\,, \tag{1}$$

where $C_g(t)$ and $C_e(t)$ are the probability amplitudes to occupy the corresponding bare states. This

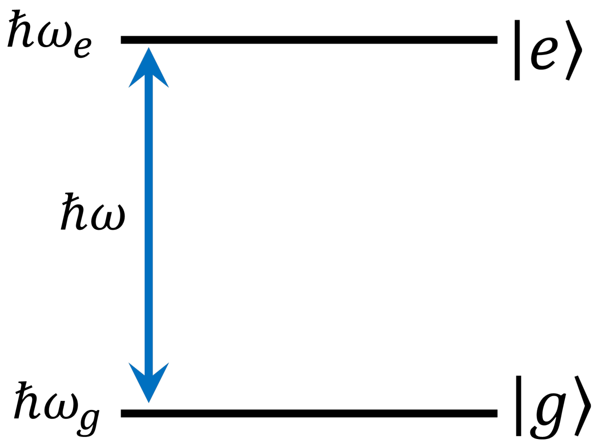

Figure 1: Schematic of the two-level atomic system

wave function will evolve over time with the dynamics governed by the time-dependent Schrödinger equation (TDSE):

$$i\hbar\frac{\partial}{\partial t}\,|\psi(t)\rangle = \hat{H}\,|\psi(t)\rangle\,, \tag{2}$$

where $i = \sqrt{-1}$ is the imaginary number, and $\hat{H}$ is the total Hamiltonian of the system, defined as:

$$\hat{H} = \hat{H}_0 + \hat{H}_1, \tag{3}$$

with $\hat{H}_1$ is the atom-field interaction Hamiltonian.

The expression for the unperturbed atomic Hamiltonian $\hat{H}_0$ can be obtained from its eigen-value equation

$$\hat{H}_0 \left| j \right\rangle = \hbar \omega_j \left| j \right\rangle, \tag{4}$$

where $j = \{g, e\}$, and by using the completeness relation $\hat{1} = \left| g \right\rangle \left\langle g \right| + \left| e \right\rangle \left\langle e \right|$ with $\hat{1}$ is the identity operator in the ket space spanned by $\{\left| g \right\rangle, \left| e \right\rangle\}$. From this, the unperturbed Hamiltonian is expressed as:

$$\hat{H}_0 = \hat{1}\hat{H}_0\hat{1} = \hbar\omega_g \left| g \right\rangle \left\langle g \right| + \hbar\omega_e \left| e \right\rangle \left\langle e \right|. \tag{5}$$

Furthermore, the interaction Hamiltonian under the *dipole approximation* is expressed as the following [36]:

$$\hat{H}_1 = -\hat{\vec{Q}} \cdot \vec{E}(t) = -\left(Q_{ge} \left| g \right\rangle \left\langle e \right| + Q_{ge}^{*} \left| e \right\rangle \left\langle g \right| \right) E(t), \tag{6}$$

where $\hat{\vec{Q}} = -q \left\langle \psi(t) \right| \hat{\vec{r}} \left| \psi(t) \right\rangle$, with q is the charge of electrons and $\hat{\vec{r}}$ is the position operator, while $Q_{ge} = Q_{eg}^{*}$ is the matrix element of the dipole moment operator induced by the electric field $\vec{E}(t)$ of the laser field. Within this approximation, the light can be treated as a plane wave covering the entire atom with negligible spatial variation. Therefore, only the field located at the atom position will be considered. We also assume that the electric field polarization is aligned with the dipole moment orientation, and the electric field $E(t)$ can be written using a time-harmonic form:

$$E(t) = E_0 \cos(\omega t), \tag{7}$$

where E_0 denotes the field amplitude. It should be noted that, the field amplitude E_0, may not be a constant, for instance, a function that describes the mode field spatial distribution. Furthermore, this approximation remains valid in the case where the optical wavelength is much larger than the size of the atom.

It is beneficial to write the time-harmonic electric field in Eq. (7) as a pair of complex exponential functions, $\cos(\omega t) = \frac{1}{2}e^{i\omega t} + \frac{1}{2}e^{-i\omega t}$. This step will help us later to introduce a very useful approximation, namely the *rotating wave approximation* (RWA) in order to reduce the mathematical complexity of the problem even further. The total Hamiltonian in terms of complex exponential functions reads:

$$\begin{aligned}\hat{H} &= \hat{H}_0 + \hat{H}_1 \\ &= \hbar\omega_g \left| g \right\rangle \left\langle g \right| + \hbar\omega_e \left| e \right\rangle \left\langle e \right| - \frac{\hbar\Omega_{ge}}{2}\left(e^{i\omega t} + e^{-i\omega t}\right) \left| g \right\rangle \left\langle e \right| - \frac{\hbar\Omega_{ge}^{*}}{2}\left(e^{i\omega t} + e^{-i\omega t}\right) \left| e \right\rangle \left\langle g \right|,\end{aligned} \tag{8}$$

where we define the Rabi frequency Ω_{ge} as:

$$\Omega_{ge} = \frac{Q_{ge}E_0}{\hbar}. \tag{9}$$

In the next part, we will introduce the RWA to simplify the Hamiltonian in Eq. (8).

1.1.2 Interaction picture and the rotating wave approximation

Interaction picture is a very useful representation in quantum mechanics, particularly to study the wave-function's time evolution due to the time-dependent interaction Hamiltonian. We can transform the wave-function in the Schrödinger picture $|\psi(t)\rangle$ to the interaction picture $|\psi_I(t)\rangle$ by defining a unitary operator $\hat{U}_0^\dagger(t)$ which satisfies [36]:

$$|\psi_I(t)\rangle = \hat{U}_0^\dagger(t)\,|\psi(t)\rangle\,, \tag{10}$$

with

$$\hat{U}_0(t) = \exp\left(-\frac{i}{\hbar}\hat{H}_0 t\right). \tag{11}$$

The TDSE in Eq. (2) can be re-written in the interaction picture as:

$$i\hbar\frac{\partial}{\partial t}\,|\psi_I(t)\rangle = \hat{\mathcal{V}}(t)\,|\psi_I(t)\rangle\,, \tag{12}$$

where $\hat{\mathcal{V}}$ is the atom-field interaction Hamiltonian in the interaction picture representation which satisfy:

$$\hat{\mathcal{V}} = \hat{U}_0^\dagger(t)\hat{H}_1\hat{U}_0(t). \tag{13}$$

In the similar manner, any operator $\hat{A}$ in Schrödinger picture will transform to interaction picture $\hat{A}_I$ as:

$$\hat{\mathcal{A}}_I = \hat{U}_0^\dagger(t)\hat{A}\hat{U}_0(t). \tag{14}$$

We will apply the interaction picture formalism to transform the Hamiltonian of two-level systems defined in the previous section. Using the atomic Hamiltonian $\hat{H}_0$ defined in Eq. (5), we define the following unitary operator:

$$\hat{U}_0 = e^{-\frac{i}{\hbar}\hat{H}_0 t} = e^{-i\omega_g t}\,|g\rangle\langle g| + e^{-i\omega_e t}\,|e\rangle\langle e|\,, \tag{15}$$

and together with Eq. (13) and the atom-field interaction Hamiltonian terms $\hat{H}_1$ of Eq. (8) we obtain:

$$\hat{\mathcal{V}} = -\frac{\hbar\Omega_{ge}}{2}\left(e^{-i\Delta t} + e^{-i(\omega+\omega_{eg})t}\right)|g\rangle\langle e| - \frac{\hbar\Omega_{ge}^*}{2}\left(e^{i\Delta t} + e^{i(\omega+\omega_{eg})t}\right)|e\rangle\langle g|\,, \tag{16}$$

where we define the transition frequency between two states $\omega_{eg} = \omega_e - \omega_g$, and the detuning between the laser frequency ω with the transition frequency ω_{eg} as $\Delta = \omega_{eg} - \omega$. Furthermore, we assumed that in our investigation, the laser field is always near to resonance with the atomic transition. This means $\Delta \ll \omega + \omega_{ge}$, such that we can keep only the slowly oscillating terms $e^{\pm i\Delta t}$, and neglect the rapidly oscillating terms $e^{\pm i(\omega+\omega_{eg})t}$ in Eq. (16), as they will vanish quicker on average compared to the terms containing Δ. This is what we called the *rotating wave approximation*. Using this approximation, the interaction Hamiltonian $\hat{\mathcal{V}}$ in Eq. (16) reduce to

$$\hat{\mathcal{V}}^{\mathrm{RWA}} \approx -\frac{\hbar\Omega_{ge}}{2}e^{-i\Delta t}\,|g\rangle\langle e| - \frac{\hbar\Omega_{ge}^*}{2}e^{i\Delta t}\,|e\rangle\langle g|\,. \tag{17}$$

After introducing the RWA in the interaction picture representation, it is possible to transform back into the Schrödinger picture by applying the inverse of Eq. (13). The transformation reads:

$$\hat{H}_1^{\mathrm{RWA}} = \hat{U}_0 \hat{\mathcal{V}}^{\mathrm{RWA}} \hat{U}_0^{\dagger} = -\frac{\hbar\Omega_{ge}}{2} e^{i\omega t} \left|g\right\rangle \left\langle e\right| - \frac{\hbar\Omega_{ge}^{*}}{2} e^{-i\omega t} \left|e\right\rangle \left\langle g\right| . \tag{18}$$

Therefore, the total Schrödinger picture Hamiltonian in the RWA is:

$$\hat{H}^{\mathrm{RWA}} = \hat{H}_0 + \hat{H}_1^{\mathrm{RWA}} = \hbar\omega_g \left|g\right\rangle \left\langle g\right| + \hbar\omega_e \left|e\right\rangle \left\langle e\right| - \frac{\hbar\Omega_{ge}}{2} e^{i\omega t} \left|g\right\rangle \left\langle e\right| - \frac{\hbar\Omega_{ge}^{*}}{2} e^{-i\omega t} \left|e\right\rangle \left\langle g\right| . \tag{19}$$

This final form of Schrödinger picture Hamiltonian under the RWA will be our main starting point later to study a more complex form of interaction, particularly, the one involving multi-level atomic systems.

1.1.3 Density operator formalism

The next step is to study the dynamics or time evolution for the wave functions of the two-level system under the *dipole* and *rotating wave approximation*. Using the RWA Hamiltonian in the Schrödinger picture given by Eq. (19), the wave function's evolution can be directly solved from the TDSE in Eq. (2) together with the definition in Eq. (1) to obtain the wave function at any time $|\psi(t)\rangle$. As all of the possible information is contained in the wave function $|\psi(t)\rangle$, any information of physical quantities represented by an operator $\hat{A}$ can be extracted by taking its expectation value in state $|\psi(t)\rangle$ as:

$$\langle \hat{A} \rangle_{QM} = \left\langle \psi(t)\right| \hat{A} \left|\psi(t)\right\rangle . \tag{20}$$

However, in many practical situations, the exact wave-function or states $|\psi(t)\rangle$ is often unknown, and only the probability to occupy that state P_ψ that is known. Therefore, a statistical average of the ensemble of states that are prepared in identical manner with $|\psi(t)\rangle$ is needed to extract the physical quantity's information. The statistical average of $\hat{A}$ in an ensemble of identically prepared states $|\psi(t)\rangle$ is given by:

$$\langle \langle \hat{A} \rangle_{QM} \rangle_{\mathrm{ensemble}} = \mathrm{Tr}(\hat{A}\hat{\rho}) = \mathrm{Tr}(\hat{\rho}\hat{A}), \tag{21}$$

where we define the density operator (matrix) $\hat{\rho}$ as the following:

$$\hat{\rho} = \sum_{\psi} P_\psi \left|\psi(t)\right\rangle \left\langle \psi(t)\right| . \tag{22}$$

In a very specific case where we have a pure state $|\psi_0(t)\rangle$, that is the states with probability $P_{\psi_0} = 1$ while the other states have zero probabilities, the density operator become:

$$\hat{\rho} = \left|\psi_0(t)\right\rangle \left\langle \psi_0(t)\right| . \tag{23}$$

Moreover, the probability conservation of the mixed state must be satisfied which in density operator language translates into:

$$\mathrm{Tr}(\hat{\rho}) = 1, \tag{24}$$

where for the pure state, we also have:

$$\mathrm{Tr}(\hat{\rho}^2) = 1. \tag{25}$$

In the density operator framework, the dynamics can be studied alternatively via the Liuoville-Von Neumann equation (LVNE) of motion:

$$\dot{\hat{\rho}} = -\frac{i}{\hbar}\left[\hat{H}, \hat{\rho}\right], \tag{26}$$

where the abbreviation $\dot{\hat{\rho}} = \frac{\partial \hat{\rho}}{\partial t}$ is used, and the bracketed terms on the right-hand side denotes the commutator of the Hamiltonian and the density operator. This equation of motion can be derived from the TDSE in Eq. (2), and is more general in the sense that it also contains the statistical mixture information as well. Moreover, another advantage of this formulation is that it allows us to include the decay of excited state population due to spontaneous emission or other decoherence mechanism. Whereas, within the dynamics of pure-states described by the TDSE in Eq. (2), the effect of decoherence is not included.

In order to incorporate the population decay, we re-write the equation of motion as [36]:

$$\dot{\hat{\rho}} = -\frac{i}{\hbar}\left[\hat{H}, \hat{\rho}\right] - \frac{1}{2}\left\{\hat{\Gamma}, \hat{\rho}\right\}, \tag{27}$$

where we define the relaxation operator $\hat{\Gamma}$ as:

$$\langle m|\,\hat{\Gamma}\,|n\rangle = \gamma_m \delta_{mn}, \tag{28}$$

with γ_m is the decay rate constant, and δ_{mn} is the Kronecker delta. The curly bracket terms in Eq. (27) denote the anti-commutator of the relaxation operator and the density operator which explicitly written as $\left\{\hat{\Gamma}, \hat{\rho}\right\} = \hat{\Gamma}\hat{\rho} + \hat{\rho}\hat{\Gamma}$. However it should be noted that the relaxation operator defined in Eq. (28) is not the only expression to describe the decay mechanism, as it only accommodates the spontaneous decay. Another example of relaxation operator is given in [22] which also considers the effect of ground-state collision into the decay process. In general, defining the relaxation operator itself is a more complicated task that requires its own specific investigation, which is beyond the scope of this work. In this section, we will only consider the relaxation operator defined in Eq. (28). Furthermore, using the definition in Eq. (28), we can re-write Eq. (27) in terms of the i, j-th matrix element as the following:

$$\dot{\rho}_{ij} = -\frac{i}{\hbar}\sum_k \left(H_{ik}\rho_{kj} - \rho_{ik}H_{kj}\right) - \frac{1}{2}\sum_k \left(\Gamma_{ik}\rho_{kj} + \rho_{ik}\Gamma_{kj}\right), \tag{29}$$

where the summation is done over the span of bare states. This expression will be beneficial especially for studying a much more complicated multi-level systems.

1.1.4 Optical Bloch equations for two-level systems

We will use the density operator formalism to study the dynamics of two-level systems. We can construct the density operator of two-level system using spinor notation, where the wave function in Eq. (1) can be expressed as a column and row vectors:

$$|\psi(t)\rangle = \begin{pmatrix} C_g \\ C_e \end{pmatrix}; \quad \langle\psi(t)| = \begin{pmatrix} C_g^* & C_e^* \end{pmatrix}, \tag{30}$$

where for brevity we wrote $C_j(t) = C_j$, but keep in mind that the coefficients C_j are time dependent functions. Next, the density operator can be obtained by a simple matrix multiplication as the following:

$$\hat{\rho} = |\psi(t)\rangle\langle\psi(t)| = \begin{pmatrix} C_g \\ C_e \end{pmatrix}\begin{pmatrix} C_g^* & C_e^* \end{pmatrix} = \begin{pmatrix} |C_g^2| & C_g C_e^* \\ C_g^* C_e & |C_e|^2 \end{pmatrix}, \tag{31}$$

or equivalently in the Dirac notation as:

$$\hat{\rho} = \rho_{gg}|g\rangle\langle g| + \rho_{ge}|g\rangle\langle e| + \rho_{eg}|e\rangle\langle g| + \rho_{ee}|e\rangle\langle e|. \tag{32}$$

where the ρ_{ij} $(i, j = \{g, e\})$ coefficients are the matrix elements of the density operator

$$\rho_{gg} = |C_g|^2; \quad \rho_{ge} = C_g C_e^*; \quad \rho_{eg} = \rho_{ge}^*; \quad \rho_{ee} = |C_e|^2. \tag{33}$$

The diagonal elements of the density operator represents the probability of occupying the states $|g\rangle$ and $|e\rangle$, that is related to the population of atomic bare states. The off-diagonal elements represent the coherence between the atomic bare states and they depend on the relative phase between the sub-system's wave function (wave functions of the individual atomic bare states).

Now, the dynamics of each density operator's elements in two level-system can be studied using the Liouville-Von Neumann equations. Using the matrix elements form in Eq. (29), together with the RWA Hamiltonian obtained in Eq. (19) and the relaxation operator defined in Eq. (28), we obtained coupled differential equations for two-level system as:

$$\dot{\rho}_{gg} = -\gamma_g \rho_{gg} + \frac{1}{2}\left(\Omega_{ge}\rho_{eg}e^{i\omega t} - \text{c.c.}\right), \tag{34a}$$

$$\dot{\rho}_{ee} = -\gamma_e \rho_{ee} - \frac{1}{2}\left(\Omega_{ge}\rho_{eg}e^{i\omega t} - \text{c.c.}\right), \tag{34b}$$

$$\dot{\rho}_{ge} = (i\omega_{eg} - \gamma_{ge})\rho_{ge} + \frac{i\Omega_{ge}e^{i\omega t}}{2}\left(\rho_{ee} - \rho_{gg}\right), \tag{34c}$$

where c.c. denotes the complex conjugates, and $\gamma_{ge} = \gamma_{eg} = \frac{\gamma_e + \gamma_g}{2}$. The equation for $\dot{\rho}_{eg}$ can be obtained by taking the complex conjugate of Eq. (34c). These set of coupled differential equations are also called the optical Bloch equations.

Although, the Bloch equations we have obtained are defined for two-level systems, the generalization into the higher multi-level atomic systems is very straight forward with the similar manner of derivations. In the next part, we will introduce one of the well known three-level system called the Λ scheme and derive the Bloch equations for this scheme using the methods we have introduced so far. This model is very important due to its simplicity, yet it opened a range of novel phenomena such as the EIT.

1.2 Three-level system: Λ type configuration

1.2.1 Atom-fields Hamiltonian for Λ scheme

Consider a three-level system with two ground states $|g_1\rangle$ and $|g_2\rangle$, and an excited state $|e\rangle$. A weak laser field called the probe field with frequency ω_p and amplitude ϵ_p couples the $|g_1\rangle \to |e\rangle$ transition. A secondary laser field called the control field with ω_c and amplitude ϵ_c the $|g_2\rangle \to |e\rangle$ transition. This configuration is called the Λ scheme as depicted in Fig. 2, and the wave function can be written with the bare states basis as:

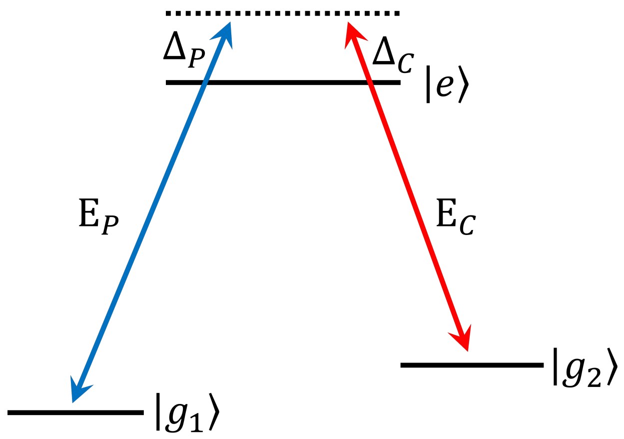

Figure 2: Schematic of the three-level atomic system forming a Λ-scheme. The excited state $|e\rangle$ is coupled to the ground states $|g1\rangle$ and $|g2\rangle$ by a probe beam E_p and control beam E_c respectively.

$$|\psi(t)\rangle = C_{g_1}(t)\,|g_1\rangle + C_{g_2}(t)\,|g_2\rangle + C_e(t)\,|e\rangle\,. \tag{35}$$

The total Hamiltonian for this Λ scheme can be written in the similar manner as the two-level system using Eq. (2), where the atomic Hamiltonian $\hat{H}_{0,\Lambda}$ written in the three-level bare states read:

$$\hat{H}_{0,\Lambda} = \hbar\omega_{g_1}\,|g_1\rangle\,\langle g_1| + \hbar\omega_{g_2}\,|g_2\rangle\,\langle g_2| + \hbar\omega_e\,|e\rangle\,\langle e|\,, \tag{36}$$

with $\hbar\omega_j$, $j = \{g_1, g_2, e\}$ are the eigen-values for the bare states. The atom-field interaction Hamiltonian $\hat{H}_{1,\Lambda}$ under the *dipole approximation* is expressed as:

$$\hat{H}_{1,\Lambda} = -\hat{\vec{Q}}_\Lambda \cdot \left(\vec{E}_p(t) + \vec{E}_c(t)\right), \tag{37}$$

where $\hat{\vec{Q}}_\Lambda$ is the dipole moment operator in the Λ scheme, while the electric fields of the probe $E_p(t)$ and control $E_c(t)$ is expressed as:

$$\vec{E}_j(t) = \frac{1}{2}\epsilon_j\vec{e}_j e^{-i\omega_j t} + \text{c.c.}, \tag{38}$$

with $j = \{p, c\}$ and $\vec{e}_j$ is the field polarization's unit vector. We assumed that the polarization of the probe and control fields are orthogonal to each other $\left(\vec{e}_p \cdot \vec{e}_c\right) = 0$. Since the control field only couples the $|g_2\rangle \rightarrow |e\rangle$ transition and the probe field only couples the $|g_1\rangle \rightarrow |e\rangle$ transition, Eq. (37) can be expressed as:

$$\hat{H}_{1,\Lambda} = -\frac{\hbar\Omega_p}{2}\left(e^{i\omega_p t} + e^{-i\omega_p t}\right)|g_1\rangle\langle e| - \frac{\hbar\Omega_c}{2}\left(e^{i\omega_c t} + e^{-i\omega_c t}\right)|g_2\rangle\langle e| + \text{H.c.}, \tag{39}$$

where H.c. denotes the Hermitian conjugates, and we defined the Rabi frequencies for the transition Ω_p and Ω_c as:

$$\Omega_p = \frac{Q_{g_1 e}\epsilon_p}{\hbar}; \quad \Omega_c = \frac{Q_{g_2 e}\epsilon_c}{\hbar}, \tag{40}$$

with $Q_{ij} = Q^*_{ji} = \langle i|\hat{Q}_\Lambda|j\rangle, (i = \{g_1, g_2\}, j = \{e\})$ is the matrix element of the dipole moment operator for the corresponding transitions in the Λ scheme.

Next, we will simplify the Hamiltonian by moving into the interaction picture and applying the RWA. From the unperturbed atomic Hamiltonian expressed in Eq. (36), we define the following unitary operator:

$$\hat{U}_{0,\Lambda} = e^{-\frac{i}{\hbar}\hat{H}_{0,\Lambda}t} = e^{-i\omega_{g_1}t}|g_1\rangle\langle g_1| + e^{-i\omega_{g_2}t}|g_2\rangle\langle g_2| + e^{-i\omega_e t}|e\rangle\langle e|. \tag{41}$$

Applying the transformation in Eq. (13) using the defined interaction Hamiltonian in Eq. (39) and the unitary operator in Eq. (41), we obtained the interaction picture Hamiltonian for the Λ scheme as:

$$\hat{\mathcal{V}}_{1,\Lambda} = -\frac{\hbar\Omega_p}{2}\left(e^{i\Delta_p t} + e^{-i(\omega_p+\omega_{eg_1})t}\right)|g_1\rangle\langle e| - \frac{\hbar\Omega_c}{2}\left(e^{i\Delta_c t} + e^{-i(\omega_c+\omega_{eg_2})t}\right)|g_2\rangle\langle e| + \text{H.c.}, \tag{42}$$

where the field detunings are defined as:

$$\Delta_p = \omega_p - \omega_{eg_1}; \quad \Delta_c = \omega_c - \omega_{eg_2}, \tag{43}$$

and the transition frequencies as:

$$\omega_{eg_1} = \omega_e - \omega_{g_1}; \quad \omega_{eg_2} = \omega_e - \omega_{g_2}. \tag{44}$$

Applying the RWA, we eliminate all the fast oscillating terms $e^{\pm i(\omega_p+\omega_{eg_1})}$ and $e^{\pm i(\omega_c+\omega_{eg_2})}$ and retain only the slow oscillating terms containing the detunings Δ_p and Δ_c. Under the RWA, Eq. (42) now reads:

$$\hat{\mathcal{V}}^{\text{RWA}}_{1,\Lambda} \approx -\frac{\hbar\Omega_p e^{i\Delta_p t}}{2}|g_1\rangle\langle e| - \frac{\hbar\Omega_c e^{i\Delta_c t}}{2}|g_2\rangle\langle e| + \text{H.c.}. \tag{45}$$

Transforming back the RWA interaction Hamiltonian in Eq. (45) into the Schrödinger picture, we obtain:

$$\hat{H}^{\text{RWA}}_{1,\Lambda} \approx -\frac{\hbar\Omega_p e^{i\omega_p t}}{2}|g_1\rangle\langle e| - \frac{\hbar\Omega_c e^{i\omega_c t}}{2}|g_2\rangle\langle e| + \text{H.c.}. \tag{46}$$

Therefore, the Schrödinger picture's total Hamiltonian of Λ scheme under the *dipole approximation* and RWA reads:

$$
\begin{aligned}
\hat{H}_{\Lambda}^{\mathrm{RWA}} &= \hat{H}_{0,\Lambda} + \hat{H}_{1,\Lambda}^{\mathrm{RWA}} \\
&= \hbar\omega_{g_1} |g_1\rangle \langle g_1| + \hbar\omega_{g_2} |g_2\rangle \langle g_2| + \hbar\omega_e |e\rangle \langle e| + \cdots \\
&\cdots - \frac{\hbar\Omega_p e^{i\omega_p t}}{2} |g_1\rangle \langle e| - \frac{\hbar\Omega_c e^{i\omega_c t}}{2} |g_2\rangle \langle e| + \mathrm{H.c.}.
\end{aligned} \tag{47}
$$

In order to reduce the complexity of the problem later when we study the equation of motions for this system, we perform another unitary transformation within the Schrödinger picture in order to remove the time-dependency of the Hamiltonian in Eq. (47). We define the following transformation:

$$
\hat{H}' = i\hbar \frac{\partial \hat{W}}{\partial t} \hat{W}^{\dagger} + \hat{W} \hat{H}^{\mathrm{RWA}} \hat{W}^{\dagger}, \tag{48}
$$

where $\hat{H}'$ is the time-independent Hamiltonian, and $\hat{H}^{\mathrm{RWA}}$ is the time-dependent RWA Hamiltonian in the Schrödinger picture. The unitary operator $\hat{W}$ acting in the transformation defined in Eq. (48) is defined by setting one of the bare states as the zero point energy. This zero point can be arbitrarily chosen between any bare states, where in this frame, the time-dependent exponential terms containing the optical frequencies ω_p and ω_c in the Hamiltonian are canceled. In other words, the transformation defined in Eq. (48) allows us to transform the Hamiltonian into the frame rotating with the optical frequency ω_p and ω_c without affecting the studied physical phenomena.

In order to apply the transformation in Eq. (48) for the Schrödinger picture's total Hamiltonian of Λ scheme defined in Eq. (47), we can choose the excited state $|e\rangle$ as our zero point energy. Within this choice of zero point energy, the unitary operator $\hat{W}$ can be defined as:

$$
\hat{W} = e^{i(\omega_e - \omega_p)t} |g_1\rangle \langle g_1| + e^{i(\omega_e - \omega_c)t} |g_2\rangle \langle g_2| + e^{i\omega_e t} |e\rangle \langle e| . \tag{49}
$$

Applying Eq. (48) with the defined unitary operator in Eq. (49) and Λ scheme Hamiltonian in Eq. (47), we obtained the time-independent Hamiltonian of Λ scheme as:

$$
\begin{aligned}
\hat{H}'_{\Lambda} &= \hbar\Delta_p |g_1\rangle \langle g_1| + \hbar\Delta_c |g_2\rangle \langle g_2| + \cdots \\
&\cdots - \frac{\hbar\Omega_p}{2} |g_1\rangle \langle e| - \frac{\hbar\Omega_c}{2} |g_2\rangle \langle e| + \mathrm{H.c.}.
\end{aligned} \tag{50}
$$

1.2.2 Optical Bloch equations for the Λ scheme

The dynamics of three-level system in the Λ scheme, can be studied in the similar manner with two-level system using the Liouville-Von Neumann equation. Moreover, we consider that the decay of populations in this system is only caused by the spontaneous emission described by the relaxation operator in Eq.(28). Therefore, using Eq. (28),(29), and (50) together we obtained the following coupled Bloch equations:

$$\dot{\rho}_{g_1g_1} = \frac{i\Omega_p}{2}\rho_{eg_1} - \frac{i\Omega_p^*}{2}\rho_{g_1e} - \gamma_{g_1}\rho_{g_1g_1}, \tag{51a}$$

$$\dot{\rho}_{g_2g_2} = \frac{i\Omega_c}{2}\rho_{eg_2} - \frac{i\Omega_c^*}{2}\rho_{g_2e} - \gamma_{g_2}\rho_{g_2g_2}, \tag{51b}$$

$$\dot{\rho}_{ee} = \frac{i\Omega_p^*}{2}\rho_{g_1e} - \frac{i\Omega_p}{2}\rho_{eg_1} + \frac{i\Omega_c^*}{2}\rho_{g_2e} - \frac{i\Omega_c}{2}\rho_{eg_2} - \gamma_e\rho_{ee}, \tag{51c}$$

$$\dot{\rho}_{g_1g_2} = \left(i(\Delta_c - \Delta_p) - \gamma_{g_1g_2}\right)\rho_{g_1g_2} + \frac{i\Omega_p}{2}\rho_{eg_2} - \frac{i\Omega_c^*}{2}\rho_{g_1e}, \tag{51d}$$

$$\dot{\rho}_{g_1e} = \left(i\Delta_p - \gamma_{g_1e}\right)\rho_{g_1e} + \frac{i\Omega_p}{2}\left(\rho_{ee} - \rho_{g_1g_1}\right) - \frac{i\Omega_c}{2}\rho_{g_1g_2}, \tag{51e}$$

$$\dot{\rho}_{g_2e} = -\left(i\Delta_c + \gamma_{g_2e}\right)\rho_{g_2e} + \frac{i\Omega_c}{2}\left(\rho_{ee} - \rho_{g_2g_2}\right) - \frac{i\Omega_c}{2}\rho_{g_2g_1}, \tag{51f}$$

where $\gamma_{ij} = \frac{\gamma_i+\gamma_j}{2}$ $(i, j \in \{g_1, g_2, e\},\ i \neq j)$ represent the decay rates of the population-coherence terms ρ_{ij}, and γ_j $(j \in \{g_1, g_2, e\})$ represent the decay rates for the bare-state populations ρ_{jj}. The equations of motion for the remaining coherence terms $\dot{\rho}_{g_2g_1}$, $\dot{\rho}_{eg_1}$, and $\dot{\rho}_{eg_2}$, can be obtained by taking the complex conjugate of Eqs. (51d)-(51f).

In order to analytically solve Eqs. (51a) - Eqs.(51f) we will use two assumptions. First, we assume that the interaction between the laser fields with the considered atomic system has reached its steady-state regime. In this regime, all the time derivatives can be assumed to be zero, meaning that each density-matrix element is constant over time. Second, we assume the weak probe field limit $\Omega_p \ll \Omega_c$ where the probe field strength is too small to drive the transition from the ground state $|g_1\rangle$ to the excited state $|e\rangle$. Within this limit, we can assume that if the atom is initially in the state $|g_1\rangle$, the other states will remain unpopulated, such that $\rho_{g_1g_1} \approx 1$ and $\rho_{g_2g_2}, \rho_{ee} \approx 0$. Under these assumptions, we can obtain the following coupled equations:

$$0 = \left(i(\Delta_c - \Delta_p) - \gamma_{g_1g_2}\right)\rho_{g_1g_2} - \frac{i\Omega_c^*}{2}\rho_{g_1e}, \tag{52a}$$

$$0 = \left(i\Delta_p - \gamma_{g_1e}\right)\rho_{g_1e} - \frac{i\Omega_p}{2} - \frac{i\Omega_c}{2}\rho_{g_1g_2}, \tag{52b}$$

where the matrix element $\rho_{g_2e} \approx 0$ due to the unpopulated excited state $|e\rangle$ and ground state $|g_2\rangle$ in the used assumption. These equations together can be solved to obtain ρ_{g_1e} and $\rho_{g_1g_2}$ as the following:

$$\rho_{g_1e} = \frac{\Omega_p(\Delta_c - \Delta_p + i\gamma_{g_1g_2})}{4(\Delta_p + i\gamma_{g_1e})(\Delta_c - \Delta_p + i\gamma_{g_1g_2}) - |\Omega_c|^2}, \tag{53a}$$

$$\rho_{g_1g_2} = \frac{\Omega_c^*\Omega_p/2}{4(\Delta_p + i\gamma_{g_1e})(\Delta_c - \Delta_p + i\gamma_{g_1g_2}) - |\Omega_c|^2}, \tag{53b}$$

where for simplification later, we can assume that $\Omega_j^* = \Omega_j$ $(j \in p, c)$.

1.2.3 Susceptibility for Λ scheme

One of the main parameters that affects the light propagation inside a medium is the medium's susceptibility χ, which is directly related to the medium's complex polarization density $\vec{\mathcal{P}}$. If we consider a medium of atomic gases with the numbers of atoms per unit volume, N, then the total medium's complex polarization density can be related to the ensemble average of the atomic dipole moment $\left\langle \langle \hat{\vec{Q}} \rangle_{QM} \right\rangle_{\text{ensemble}}$ as the following [36]:

$$\vec{\mathcal{P}} = N \left\langle \langle \hat{\vec{Q}} \rangle_{QM} \right\rangle_{\text{ensemble}} = N \operatorname{Tr}(\hat{\rho}\hat{\vec{Q}}). \tag{54}$$

Whereas, the relations between the complex polarization density $\vec{\mathcal{P}}$, susceptibility χ, and the electric field that induced the dipole moments $\vec{E}$ is given by:

$$\vec{\mathcal{P}} = \varepsilon_0 \chi \vec{E}, \tag{55}$$

where ε_0 is a vacuum permittivity constant. In particular for the Λ scheme we have considered, Eq. (55) can be rewritten as the following:

$$\vec{\mathcal{P}} = \varepsilon_0 \chi_p \vec{E}_P + \varepsilon_0 \chi_c \vec{E}_c, \tag{56}$$

where χ_j $(j = p, c)$ is the susceptibility for the corresponding laser field E_j.

To obtain the exact relation between the susceptibilities with the corresponding dipole moment and driving electric fields component, we can write Eq. (54) in their matrix form:

$$\vec{\mathcal{P}} = N \operatorname{Tr}\left(\begin{bmatrix} \rho_{g_1g_1} & \rho_{g_1g_2} & \rho_{g_1e} \\ \rho_{g_2g_1} & \rho_{g_2g_2} & \rho_{g_1e} \\ \rho_{eg_1} & \rho_{eg_2} & \rho_{ee} \end{bmatrix} \begin{bmatrix} 0 & 0 & \vec{e}_p Q_{g_1e} \\ 0 & 0 & \vec{e}_c Q_{g_2e} \\ \vec{e}_p Q_{eg_1} & \vec{e}_c Q_{eg_1} & 0 \end{bmatrix} \right), \tag{57}$$

where $\vec{e}_j$ $(j \in \{p, c\})$ is the unit vector for the induced dipole moment which aligned with the probe and control fields polarization. Taking the trace of matrix multiplication in Eq. (57), we obtained:

$$\vec{\mathcal{P}} = N \left(Q_{g_1e}\rho_{eg_1} + Q_{eg_1}\rho_{g_1e} \right) \vec{e}_p + N \left(Q_{g_2e}\rho_{eg_2} + Q_{eg_2}\rho_{g_2e} \right) \vec{e}_c. \tag{58}$$

Moving to an appropriate rotating frame that oscillates with the driving laser frequencies ω_p and ω_c defined by Eq. (49), we can re-write the density operator elements in this frame using the following transformation:

$$\hat{\rho}' = \hat{W}\hat{\rho}\hat{W}^\dagger. \tag{59}$$

Within this rotating frame, the new density operator elements that correspond to the induced dipole elements in Eq. (58) are obtained as:

$$\rho'_{eg_1} = \rho_{eg_1} e^{i\omega_p t}, \tag{60a}$$

$$\rho'_{eg_2} = \rho_{eg_2} e^{i\omega_c t}. \tag{60b}$$

Such that, Eq. (58) can be re-written as the following:

$$\vec{\mathcal{P}} = N\left(Q_{g_1e}\rho'_{eg_1}e^{-i\omega_p t} + Q_{eg_1}\rho'_{g_1e}e^{i\omega_p t}\right)\vec{e}_p + N\left(Q_{g_2e}\rho'_{eg_2}e^{-i\omega_c t} + Q_{eg_2}\rho'_{g_2e}e^{i\omega_c t}\right)\vec{e}_c. \tag{61}$$

Whereas, using the time-harmonic form of the electric field in Eq. (38), we can re-write Eq. (56) as the following:

$$\vec{\mathcal{P}} = \varepsilon_0\chi_p\frac{\vec{e}_p}{2}\left(\epsilon_p e^{i\omega_p t} + \epsilon_p^* e^{-i\omega_p t}\right) + \varepsilon_0\chi_c\frac{\vec{e}_c}{2}\left(\epsilon_c e^{i\omega_c t} + \epsilon_c^* e^{-i\omega_c t}\right). \tag{62}$$

Therefore, from Eq. (61) and Eq.(62) together we obtained:

$$\chi_p = \frac{2NQ_{g_1e}}{\varepsilon_0\epsilon_p}\rho'_{eg_1}, \tag{63}$$

In the steady-state regime, the time dependency in Eqs. (60a)-(60b) is omitted, so that $\rho_{ij} = \rho'_{ij}$ $(i \in \{g_1, g_2\}, j = e)$ in Eq. (63). Moreover, together with the definition of the Rabi frequency in Eq. (40), we can re-write Eq. (63) as the following:

$$\chi_p = \frac{2N|Q_{g_1e}|^2}{\hbar\varepsilon_0\Omega_p}\rho_{eg_1}, \tag{64}$$

Finally, by using the density operator element ρ_{g_1e} obtained in Eq. (53a), we obtained the susceptibility affecting the propagation of the weak probe χ_p as:

$$\chi_p = \frac{2N|Q_{g_1e}|^2}{\hbar\varepsilon_0}\frac{\Delta_c - \Delta_p + i\gamma_{g_1g_2}}{4(\Delta_p + i\gamma_{g_1e})(\Delta_c - \Delta_p + i\gamma_{g_1g_2}) - |\Omega_c|^2}. \tag{65}$$

1.2.4 Electromagnetically induced transparency (EIT) in Λ scheme: *dark state* picture

In this section, we will discuss one of the most important phenomena obtained from the weak probe limit in the Λ scheme we have derived previously, called the electromagnetically induced transparency (EIT). This phenomenon allows the initially opaque medium at the probe wavelength to become transparent due to quantum coherence when the strong control field is present [9]. To explain the quantum coherence, we will first introduce the notion of *dark state* in Λ scheme, that is, a quantum superposition of atomic states that does not interact with the laser field excitations [37].

To find the dark state of the Λ scheme, we consider the simplest case of two-photon resonance, in which $\Delta_p = \Delta_c = \Delta$. This way, the rotating wave Hamiltonian of Λ scheme in Eq. (50) can be written in the matrix form as [11]:

$$\hat{H}'_\Lambda = \frac{\hbar}{2}\begin{bmatrix} 2\Delta & 0 & -\Omega_p \\ 0 & 2\Delta & -\Omega_c \\ -\Omega_p^* & -\Omega_c^* & 0 \end{bmatrix}. \tag{66}$$

Via diagonalization, the eigen-states of the Hamiltonian in Eq. (66) can be written in the basis of atomic bare states $|g_1\rangle$, $|g_2\rangle$, and $|e\rangle$ as the following:

$$|d\rangle = \cos\Theta\,|g_1\rangle - \sin\Theta\,|g_2\rangle\,, \tag{67a}$$

$$|+\rangle = \sin\Phi\,(\sin\Theta\,|g_1\rangle + \cos\Theta\,|g_2\rangle) + \cos\Phi\,|e\rangle\,, \tag{67b}$$

$$|-\rangle = \cos\Phi\,(\sin\Theta\,|g_1\rangle + \cos\Theta\,|g_2\rangle) - \sin\Phi\,|e\rangle\,, \tag{67c}$$

that corresponds to the eigenvalues:

$$\lambda_d = \Delta, \tag{68a}$$

$$\lambda_\pm = \frac{\Delta \pm \sqrt{\Delta^2 + \Omega^2}}{2}. \tag{68b}$$

The mixing angles Θ and Φ, are defined as:

$$\tan\Theta = \frac{|\Omega_p|}{|\Omega_c|}, \tag{69a}$$

$$\tan\Phi = \frac{\Delta}{\Delta + \sqrt{\Delta^2 + \Omega^2}}, \tag{69b}$$

where the normalized Rabi frequency Ω is defined as:

$$\Omega = \sqrt{|\Omega_p|^2 + |\Omega_c|^2}. \tag{70}$$

From Eqs. (67a)-(67c), it is shown that both the eigen-states $|\pm\rangle$ consist of the superposition from all the atomic bare states $|g_1\rangle$, $|g_2\rangle$, and $|e\rangle$. However the eigen-state $|d\rangle$ only formed from the superposition of two lower state $|g_1\rangle$ and $|g_2\rangle$, making transition $|d\rangle \to |e\rangle$ not possible. This means, the eigen-state $|d\rangle$ cannot interact with light, and thus called the *dark state*.

The description of the *dark state* can be further simplified in the weak-probe limit to make it more apparent which laser field cannot interact with the atom. By assuming $\Omega_p \ll \Omega_c$ in the weak probe limit, we have $\cos\Theta \to 1$ and $\sin\Theta \to 0$. Furthermore, we assume that the atom is on resonance with the laser fields ($\Delta = 0$), such that $\tan\Phi \to 1$ ($\Phi = \pi/4$). Therefore, from Eqs. (67a)-(67c) we have

$$|d\rangle \approx |g_1\rangle\,, \tag{71a}$$

$$|+\rangle \approx \frac{|g_2\rangle + |e\rangle}{\sqrt{2}}, \tag{71b}$$

$$|-\rangle \approx \frac{|g_2\rangle - |e\rangle}{\sqrt{2}}, \tag{71c}$$

where it is apparent that within these two assumptions, the atomic bare state $|g_1\rangle$ is now the *dark state*, while the bare state $|g_2\rangle$ allows a transition to the excited state $|e\rangle$. Consequently, the medium interacts only with the control field while becoming transparent to the probe field.

1.2.5 Electromagnetically induced transparency (EIT) in Λ scheme: density operator picture

Although the description of *dark state* can explain the EIT intuitively, this description is incomplete since it does not involve the effect of the decay of population and coherence. Therefore, employing the density operator formalism is necessary to obtain the more accurate description of EIT which is also affected by decay such as spontaneous emission. In the density operator formalism of Λ scheme that includes the spontaneous emission as the main decay mechanism, we obtained the susceptibility for the weak probe field in Eq. (65). From the obtained susceptibility, the absorption spectrum that corresponds to the imaginary part of the susceptibility $\mathrm{Im}(\chi_p)$ can be plotted against the probe detuning Δ_p.

To plot the absorption, we consider an ideal case of EIT where the ground states $|g_1\rangle$ and $|g_2\rangle$ are assumed to be meta-stable with very long lifetime. Therefore $\gamma_{g_1} = \gamma_{g_2} = \gamma_{g_1 g_2} = 0$. We also assumed that the control field is on resonance with the $|g_2\rangle \rightarrow |e\rangle$ transition $\Delta_c = 0$. In this assumption, Eq. (65) is simplified into:

$$\chi_p = \frac{2N|Q_{g_1 e}|^2}{\hbar\varepsilon_0} \frac{\Delta_p}{4\Delta_p(\Delta_p + i\gamma_{g_1 e}) + |\Omega_c|^2}. \tag{72}$$

Figure 3 shows the absorption and dispersion spectra of Λ scheme for different cases of control field strength $|\Omega_c|$. From the plot, it can be seen that without the control field present ($\Omega_c = 0$), the probe field experience the highest absorption on resonance $\Delta_p = 0$. However, when a control field is turned on ($\Omega_c = \gamma$), the peak of absorption splits and opens a transparency window on resonance with zero absorption. This means, the probe field at the exact frequency that match the $|g_1\rangle \rightarrow |e\rangle$ transition will propagate without loss. Furthermore, with stronger control field ($\Omega_c = 5\gamma$), the transparency window broadens, allowing different values of probe frequencies to propagate without loss in the previously opaque medium. This phenomenon of transparency window formation due to the presence of stronger secondary coherent laser radiation is called the electromagnetically induced transparency (EIT).

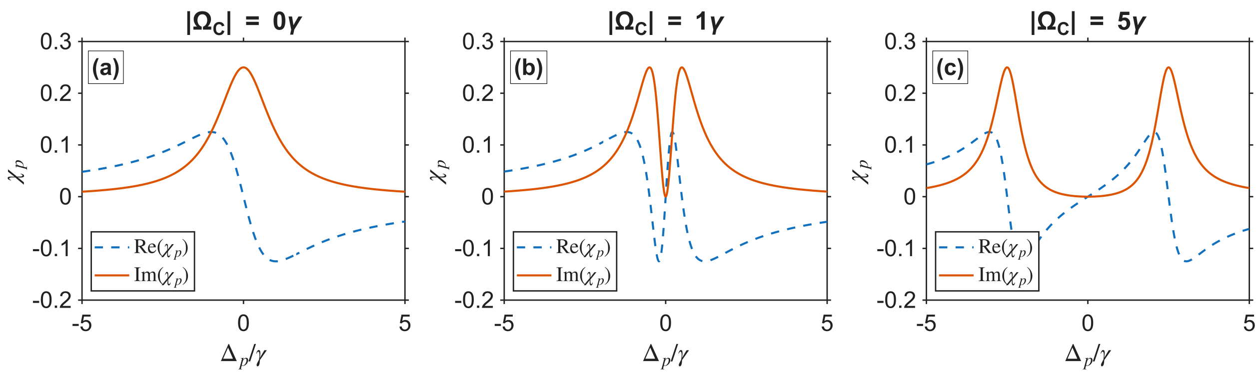

Figure 3: Absorption ($\mathrm{Im}(\chi_p)$) and dispersion ($\mathrm{Re}(\chi_p)$) spectra of Λ scheme in the weak probe limit for different cases of control field strength Ω_c as a function of Δ_p. The plot is normalized to the atomic parameters and physical constants $\frac{2N|Q_{g_1 e}|^2}{\hbar\varepsilon_0}$. The detuning Δ_p, and control field strength Ω_c are normalized to the decay rates $\gamma_{g_1 e} = \gamma$.

1.2.6 Slow light

The presence of the strong control field Ω_C in the three-level atomic system in Λ configuration previously not only modifies the absorption properties but also affects the dispersion properties of the medium. The dispersion determines how pulses with different wavelengths propagate inside the medium. The dispersion profile of the Λ atomic system is illustrated in Fig. 3, where the blue dashed lines in each plot correspond to the real part of the susceptibility. In the region close to the resonance, $\Delta_p/\gamma \approx 0$, the plot of the real part for the susceptibility shows a positive slope when the control field is present, as shown in Figs. 3(b) and 3(c). This positive slope of dispersion indicates the phenomenon of slow-light propagation [38]. The slope of dispersion directly affects the group velocity of light inside the medium according to [38, 39]:

$$v_g = \frac{\mathrm{d}\omega}{\mathrm{d}k} = \frac{c}{n(\omega_p) + \omega_p \frac{\mathrm{d}n}{\mathrm{d}\omega}|_{\omega_{0j}}} = \frac{c}{1 + \frac{c\pi}{\lambda_p}\mathrm{Re}\left[\frac{\partial \chi_p}{\partial \omega}|_{\omega_{0j}}\right]}, \tag{73}$$

where v_g denotes the group velocity of the light pulse, and $k = \frac{\omega n}{c}$ is the wave number of light inside the medium. Here, $n(\omega_p)$ is the refractive index of the medium for a probe light with optical frequency ω_p and wavelength λ_p, while ω_{0j} is the central frequency of the atomic transition. Equation (73) implies that a very steep slope of dispersion corresponds to a lower group velocity due to the larger denominator term, leading to slower propagation of light pulses.

In the EIT-based slow-light system, the reduction of the group velocity depends on the formation of the transparency window, in particular, the width of the transparency window. As can be seen in Figs. 3(b) and 3(c), the steepness of the dispersion curves decreases as the separation between the absorption peaks increases. By reducing the intensity of the control field, the transparency window becomes narrower, and the slope of dispersion become steeper. A group velocity as low as 17 m/s was experimentally achieved in 1999 using a system of ultracold sodium gas coupled to a very weak control field [26]. Since then, extensive investigation has been carried out, paving the way towards many applications, inclduing the enhancement of optical nonlinearities [29, 31, 40], and even stored light [10, 32], which has promising applications in atomic quantum memories for storing information carried by light.

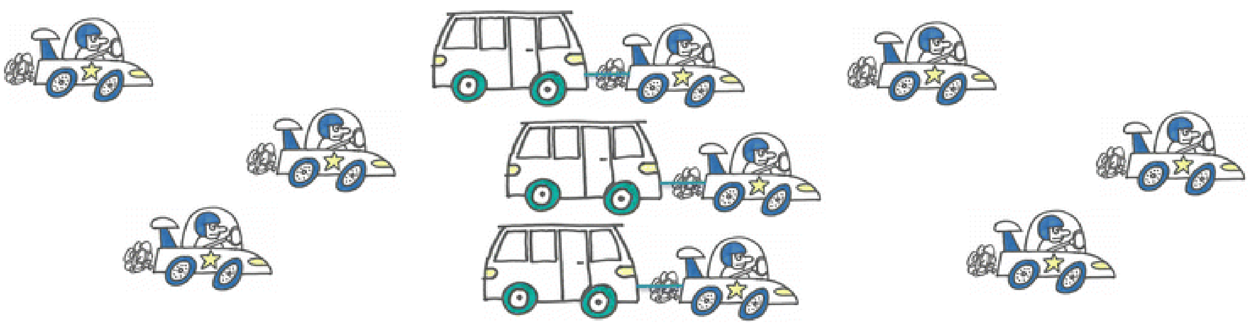

Figure 4: A simple picture of slow light where the fast small cars represent photons propagating, and bigger heavy trailers represent atomic excitations [38].

To provide a more intuitive description on how an atomic medium can be used to slow down light, consider the illustration of fast-moving cars and trailers in Fig. 4 taken from [38]. One can visualize the propagating photons as fast-moving small cars traveling in vacuum. When the photons enter the atomic medium, most of the photons are converted into an atomic excitations, which cannot move on their own, as such it can be visualized as a large, heavy trailers. These excitations are then coupled to the remaining photons, as if the remaining small cars are pulling many heavy trailers inside the medium, thus, slowing down the movement of the coupled car-trailer system. However, once this coupled car-trailer system reaches the exit of the medium, the heavy trailers (atomic excitation) are converted back into fast cars (photons). Therefore, the light exiting the medium travels back at its initial propagation speed before entering the medium.

1.3 Linear pulse propagation

1.3.1 Electromagnetic wave equations in homogeneous media

The propagation of electromagnetic waves in electrically neutral medium within the classical picture is mainly governed by the Maxwell equations [36]:

$$\nabla \cdot \vec{D} = 0, \tag{74a}$$

$$\nabla \cdot \vec{B} = 0, \tag{74b}$$

$$\nabla \times \vec{E} = -\frac{\partial \vec{B}}{\partial t}, \tag{74c}$$

$$\nabla \times \vec{H} = \vec{J} + \frac{\partial \vec{D}}{\partial t}, \tag{74d}$$

where $\vec{E}$ and $\vec{H}$ respectively are the electric and magnetic fields, $\vec{D}$ and $\vec{H}$ respectively are the electric and magnetic flux densities, and $\vec{J}$ is the electric current density. We assume the medium is non-conductive and non-magnetic such that the following constitutive relation applies:

$$\vec{D} = \varepsilon_0 \vec{E} + \vec{\mathcal{P}}, \quad \vec{B} = \mu_0 \vec{H}, \quad \vec{J} = 0, \tag{75}$$

where μ_0 denotes the vacuum magnetic permeability. In this case, the electromagnetic waves propagation through the medium will be mainly controlled by the medium susceptibility χ through the to the polarization density $\vec{\mathcal{P}}$. Furthermore, from Eqs. (74a)-(74d) altogether, we can obtain the electromagnetic waves equations written for the electric field components:

$$\nabla^2 \vec{E} - \frac{1}{c^2} \frac{\partial^2 \vec{E}}{\partial t^2} = \mu_0 \frac{\partial^2 \vec{\mathcal{P}}}{\partial t^2}, \tag{76}$$

where $c = \frac{1}{\sqrt{\varepsilon_0 \mu_0}}$ is the speed of light in vacuum. It should be noted that in Eq. (76) the medium which consist of an ensemble of atoms is considered as an homogeneous medium such that Eq.(74a) implies $\nabla \cdot \vec{E} = 0$.

1.3.2 Paraxial and slowly varying envelope approximation

To simplify the electromagnetic waves equation into a pulse propagation equations in linear regime, we will introduce the *paraxial approximation* and the *slowly varying envelope approximation* (SVEA). Assuming that the wave mainly propagates along the z direction, and has a finite extent of field in the $x-y$ plane, we can write the electric field as:

$$\vec{E}(\vec{r},t) = \vec{e}E(z,t), \tag{77}$$

where $\vec{e}$ is the unit vector of polarization that is perpendicular to the wave vector along the z direction, $\vec{k} \approx \vec{k}_z = k\vec{e}_z$. Here, we have omitted the $x-$ and $y-$ dependence of the electric-field amplitude distribution and assumed that the wave-vector components $\vec{k}_x$ and $\vec{k}_y$ are negligible to the z wave vector component $\vec{k}_z$ ($\vec{k}_x, \vec{k}_y \ll \vec{k}_z$). This assumption is called the *paraxial approximation*, and typically a valid approximation for a well collimated laser beam with low diffraction effect. Under this assumption, we can re-write the wave equations in Eq. (76) as:

$$\frac{\partial^2 E}{\partial z^2} - \frac{1}{c^2}\frac{\partial^2 E}{\partial t^2} = \mu_0 \frac{\partial^2 \mathcal{P}}{\partial t^2}, \tag{78}$$

where together with time-harmonic evolution, the electric field in Eq. (77) and the polarization density $\mathcal{P}$ can be written explicitly as:

$$E(z,t) = \frac{1}{2}E_0(z,t)e^{i(kz-\omega t)} + \text{c.c.}, \tag{79a}$$

$$\mathcal{P}(z,t) = \frac{1}{2}\mathcal{P}_0(z,t)e^{i(kz-\omega t)}\text{c.c.}, \tag{79b}$$

where ω is the wave-frequency. It should be noted that generally, both the electric field amplitude E_0 and the polarization density amplitude $\mathcal{P}_0$ are complex functions.

Next, we will implement the *slowly varying envelope approximation* (SVEA). By subtituting Eqs. (79a)-(79b) into Eq. (78) we will obtain the following form:

$$\frac{\partial^2 E_0}{\partial z^2} + 2ik\frac{\partial E_0}{\partial z} - k^2 E_0 - \frac{1}{c^2}\frac{\partial^2 E_0}{\partial t^2} + \frac{2i\omega}{c^2}\frac{\partial E_0}{\partial t} + \frac{\omega^2}{c^2}E_0 = \mu_0\frac{\partial^2 \mathcal{P}_0}{\partial t^2} - 2i\omega\mu_0\frac{\partial \mathcal{P}_0}{\partial t} - \omega^2\mu_0\mathcal{P}_0. \tag{80}$$

In the SVEA, we assume that the phase and amplitudes of electric field and polarization density do not change abruptly on the time scale of an optical period or the length scale of an optical wavelength. This allows us to apply the following conditions [36]:

$$\frac{\partial E_0}{\partial z} \ll kE_0, \quad \frac{\partial E_0}{\partial t} \ll \omega E_0, \tag{81a}$$

$$\frac{\partial \mathcal{P}_0}{\partial z} \ll k\mathcal{P}_0, \quad \frac{\partial \mathcal{P}_0}{\partial t} \ll \omega \mathcal{P}_0, \tag{81b}$$

where together with the following dispersion relation:

$$k^2 - n^2\frac{\omega^2}{c^2} = 0, \tag{82}$$

with the refractive index $n^2 = 1 + \chi$ obtained from the relation between $\vec{\mathcal{P}}$ and $\vec{E}$ in Eq. (55), we arrive at the following equation:

$$\frac{\partial E_0}{\partial z} + \frac{1}{c}\frac{\partial E_0}{\partial t} = \frac{ik}{2\varepsilon_0}\mathcal{P}_0. \tag{83}$$

This equation is the starting point for the investigation of linear pulse propagation which will be discussed throughout this work.

1.4 Optical vector vortices

1.4.1 Optical vortex

An optical vortex is a special type of structured beams that possesses a helical phase structure $e^{il\phi}$ and exhibits a phase singularity corresponding to the topological charge l, where ϕ is the azimuthal coordinate of its transverse plane [7]. Due it this phase singularity, optical vortex exhibits a doughnut shaped intensity distributions with a point of zero intensity located at its center contrary to a bright centered Gaussian beam. The topological charge l also carries the information about the photon's orbital angular momentum (OAM), which takes discrete values $l\hbar$, where l can take any integer value [6]. Moreover, the energy of a vortex beam travel in a spiral like a rotating corkscrew, instead of a straight line during its propagation [41]. The illustration of a vortex intensity distribution and its helical wavefront for a different OAM charge l is given in Fig. 5

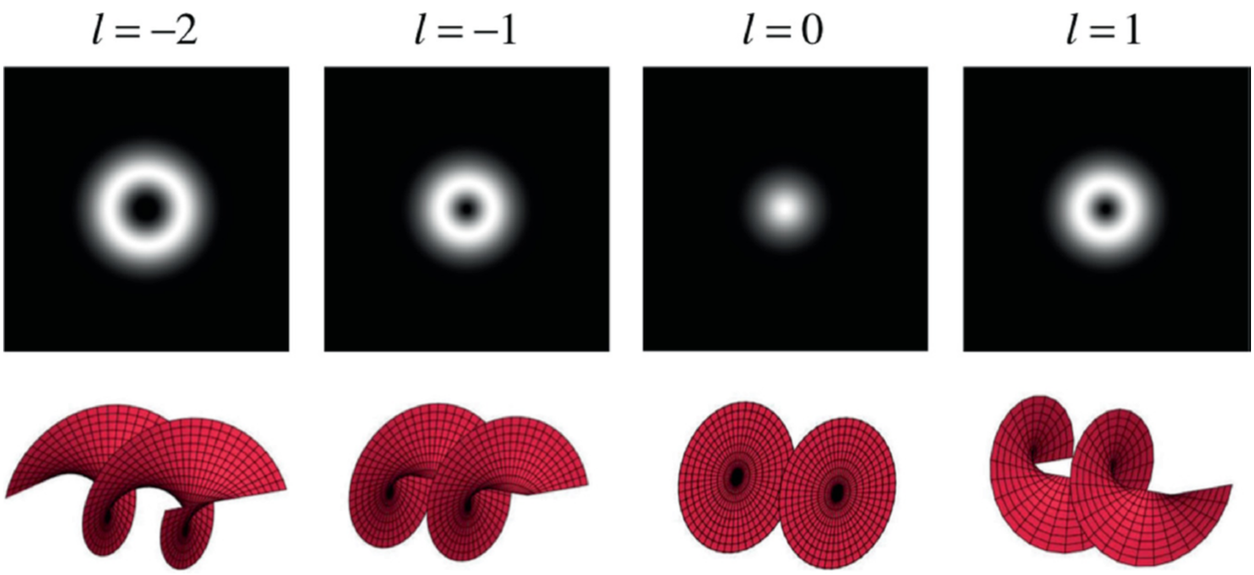

Figure 5: Illustration of intensities (top) and helical phases (down) of optical vortex for different OAM values l [41].

Mathematically, vortex beams can be represented by a Laguerre-Gaussian (LG) beam, a Bessel beam, or a Bessel-Gaussian (BG) beam [41]. All of these beams exhibit the necessary helical phase $e^{il\phi}$ that carries the vortex OAM. However, we will mainly focus on the LG beams as this beam is one of the most extensively studied one, with a wide range of applications [2–5]. The expression of LG beam is given by [41]:

$$E(r,\phi,z) = \frac{C_{p,l}}{w_0}\left(\frac{r\sqrt{2}}{w(z)}\right)^{|l|} \mathrm{LG}_p^{|l|}(\tau) e^{\frac{-r^2}{w(z)^2}} e^{il\phi} e^{i\varphi}, \tag{84}$$

where $C_{p,l}$ is a normalization constant, p is the radial mode order which can take any non-negative integers, and w_0 is the Gaussian beam waist. The beam radius position dependent beam radius $w(z)$ and phase φ are defined as:

$$w(z) = w_0\sqrt{1+\frac{z}{z_0}}, \tag{85a}$$

$$\varphi = (|l|+2p+1)\arctan\left(\frac{z}{Z_0}\right) - k\left(z+\frac{r^2}{2R}\right), \tag{85b}$$

where k denotes the wave number, z_0 denotes the Rayleigh range, and R denotes the beam curvature. These parameters are defined as:

$$z_0 = \frac{\pi w_0^2}{\lambda}, \tag{86a}$$

$$R = z + \frac{z_0^2}{z}, \tag{86b}$$

with λ denotes the wavelength. The associating Laguerre polynomial $\mathrm{LG}_p^{|l|}(\tau)$ can be expressed as:

$$\mathrm{LG}_p^{|l|}(\tau) = \sum_{m=0}^{p} \frac{(p+|l|!)(-\tau)^m}{(|l|+m)!m!(p-m)!}, \tag{87}$$

where the argument τ is defined as:

$$\tau = \frac{2r^2}{w(z)^2}. \tag{88}$$

Figure 6 shows the intensity and helical phase distribution in the transverse plane for different topological (OAM) charge l and radial mode order p of the LG beam described by Eq. (84) at $z = 0$. It can be seen that for the lowest radial mode order ($p = 0$) without OAM charge ($l = 0$) the LG beam will be reduced into ordinary Gaussian beam. As the radial mode order p increases, concentric ring-shaped intensity patterns appear, with higher p values correspond to a larger number of rings.

The generation of optical vortex can be done through various manners. One example is to use a spiral phase plates (SPP) in order to generate the helical phase patterns for a fundamental Gaussian beams. The illustration of a SPP structure is presented in Fig. 7. The helical phase induced by these plates is related to its thickness h. The thickness variation along the azimuthal angle $0 \to 2\pi$ can be related to its OAM charge l as $\Delta h = \frac{\lambda l}{n-1}$, where n is the refractive index of the plate material. However, these type of plates can only generate an optical vortex with a specific wavelength λ, and OAM charge l. This mean to generate a vortex at different wavelength or OAM charge, a new plate must be fabricated to satisfy the new requirements [41]. Alternatively, a new

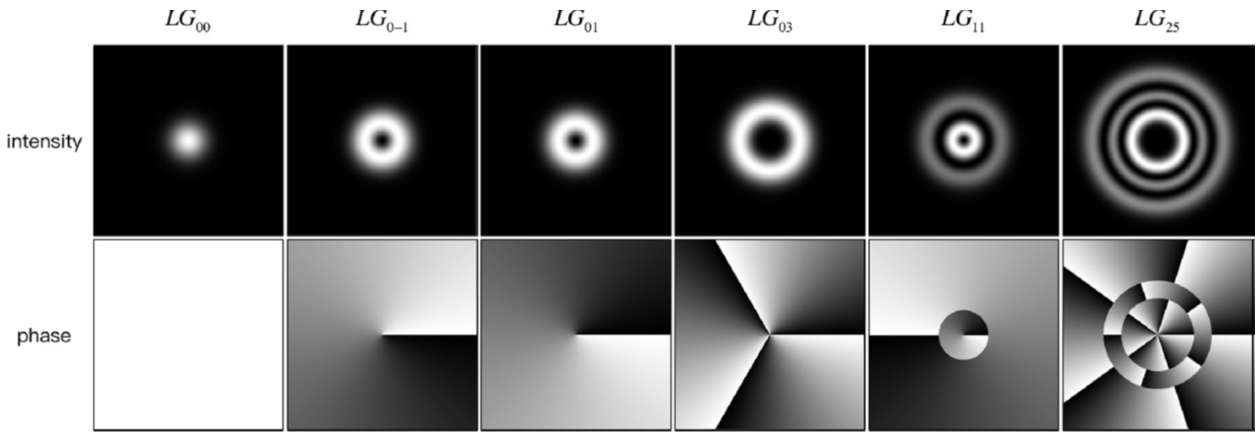

Figure 6: Intensity and phase distributions of LG beam in the transverse plane at $z = 0$ for different OAM charge l and radial mode order p [41].

type of digital laser which employs a liquid crystal spatial light modulator (LC-SLM) [42] can be used to generate various structured beam wavefronts within a single device. This device took the advantage of the programmable liquid crystal to alter the beam phase by inducing a birefringent that depends on the crystals orientation when a voltage difference is applied to the crystal. Moreover, the performance of this device is not only limited in generating various modes of LG beams, but also able to generate other type of beams such as the HG beams, flat-top beam, and Airy beam. These beams are presented in Fig. 8

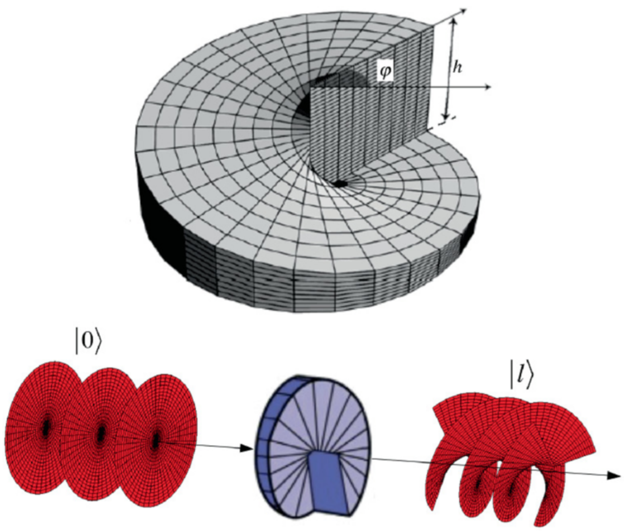

Figure 7: Sprial phase plate with thickness h (top) and transitions of Gaussian wave front into a helical wave front (down) [41].

1.4.2 Vectorial vortex beam

Vector beams can be defined as a class of optical beams which have a non-uniform polarization states distribution in its transverse plane [41]. In contrast, scalar beams possess a uniform polarization over the entire transverse plane. In the cylindrical coordinate basis, the cylindrical vector (CV) beams can exhibit an azimuthal, radial, or generalized CV (spiral like) distributions for the state of polarization (SOP) [43]. Mathematically, vector beams can be represented as a linear combinations

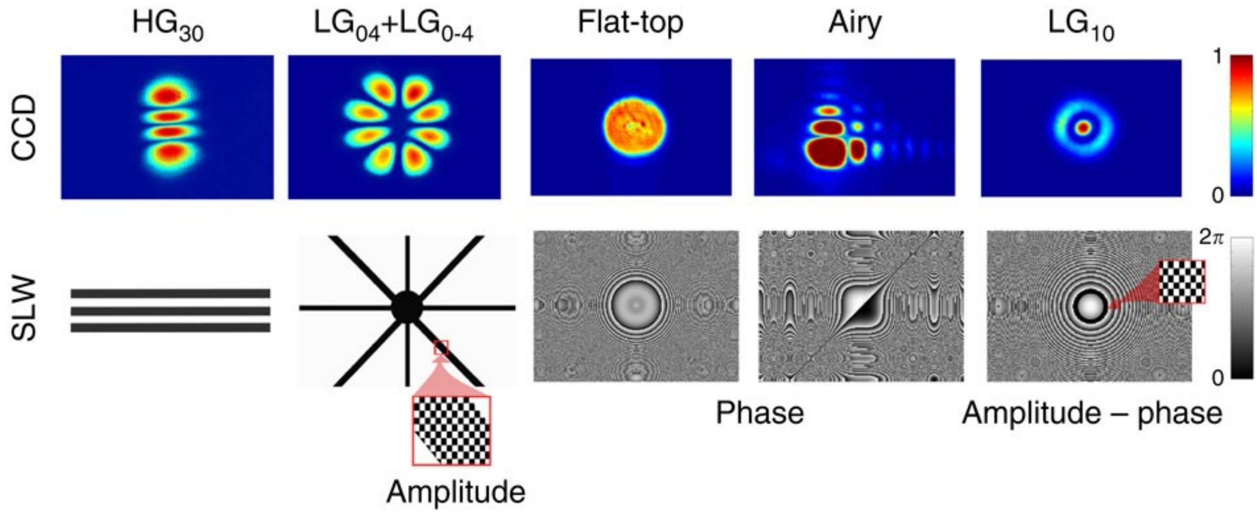

Figure 8: Various structured beams generated using the LC-SLM digital laser [42].

of two orthogonally polarized Bessel-Gaussian (BG) beams or Laguerre-Gaussian (LG) beams in the radial and azimuthal polarization basis [44,45] as:

$$\vec{E}(r,\phi,z) = \epsilon_r(r,\phi,z)\vec{e}_r + \epsilon_\phi(r,\phi,z)\vec{e}_\phi, \tag{89}$$

where $\vec{e}_r$ and $\vec{e}_\phi$ are unit vector in radial and azimuthal direction respectively, while $\epsilon_r(r,\phi,z)$ and $\epsilon_\phi(r,\phi,z)$ are the field components for the radial and azimuthal polarization that can be represented by BG or LG functions. It is also possible to construct the radial and azimuthal field components using a superposition of orthogonally polarized Hermite-Gaussian HG_{10} and HG_{10} modes [46]:

$$\epsilon_r(r,\phi,z)\vec{e}_r = \mathrm{HG}_{10}\vec{e}_x + \mathrm{HG}_{01}\vec{e}_y, \tag{90a}$$

$$\epsilon_\phi(r,\phi,z)\vec{e}_\phi = \mathrm{HG}_{01}\vec{e}_x - \mathrm{HG}_{10}\vec{e}_y. \tag{90b}$$

In short, any superposition of orthogonally polarized beams that resulted in a position dependent SOP distributions are considered as vector beams.

Figures 9(a)-9(f) show the different possibilities of linear polarization of HG_{10}, HG_{01}, and LG_{01} modes. Although these modes have different intensity distributions and particularly a phase singularity (optical vortex) for the LG_{01} mode in Fig. 9(f), they have a homogeneous polarization across the transverse plane. The polarization are uniformly vertical in Figs. 9(d)-9(e), and horizontal in Figs. 9(a)-9(c) and 9(f). In contrast, Figs. 9(g)-9(i) show SOPs that are position-dependent across the transverse plane, with vortex intensity distributions. These position dependent SOPs correspond to radial polarization (Fig.9(g)), azimuthal polarization (Fig.9(h)), and spiral polarization (Fig.9(i)). Moreover, these type of beams that show a position dependent SOPs and vortex intensity structure are called *vectorial vortex beam* (VV beam). However, it should be noted that a vector beam without a phase singularity is also possible, such as those belonging to the family of Full Poincaré (FP) beams [47].

In our case of interest, we will restrict the discussion for a VV beams constructed from a superposition of two LG beams with opposite vorticity ($+l$ and $-l$) and orthogonal circular polarizations.

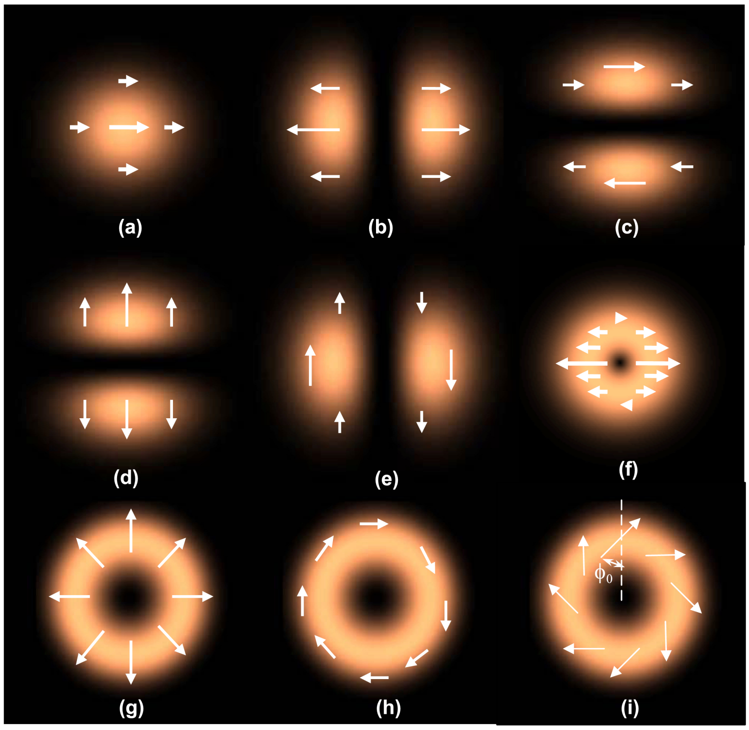

Figure 9: Examples of intensity and polarization distributions for a Gaussian, Hermite-Gaussian, and Vortex Beams. (a) Fundamental gaussian beam with horizontal polarization. (b) HG_{10} beam with horizontal polarization. (c) HG_{01} beam with horizontal polarization. (d) HG_{01} beam with vertical polarization. (e) HG_{10} beam with vertical polarization. (f) LG_{01} beam with horizontal polarization. (g) Vortex beam with radial polarization. (h) Vortex beam with azimuthal polarization. and (i) Vortex beam with spiral polarization [43].

These beams have been used in recent experiments for spatially dependent EIT [21], atomic compass [23], and, very recently, to create an atomic-state interferometer [48]. To simplify further the discussion, we consider only the lowest radial order of the LG beam $p = 0$. At the entrance of the medium $z = 0$, this beam can be expressed as the following [24]:

$$\vec{E}(r, \phi, z = 0) = E_R(r, \phi)\vec{e}_R + E_L(r, \phi)\vec{e}_L, \tag{91a}$$

$$E_R = \epsilon_R A(r) e^{il\phi}, \tag{91b}$$

$$E_L = \epsilon_L A(r) e^{-il\phi}, \tag{91c}$$

where the relative amplitudes for the right-circularly polarized (ϵ_R) and left-circularly polarized (ϵ_L) beams are defined as:

$$\epsilon_L = \varepsilon \cos(\alpha), \tag{92a}$$

$$\epsilon_R = \varepsilon e^{i\varphi} \sin(\alpha), \tag{92b}$$

with ε denotes the amplitude scaling factor, α denotes tuning angle that control the relative strength of each beams, and φ denotes the relative phase difference between the two LG modes at the entrance of the medium. The transverse profile distribution $A(r)$ is given by:

$$A(r) = \left(\frac{r}{w_0}\right)^{|l|} e^{-\frac{r^2}{w_0^2}}, \tag{93}$$

with w_0 is the radius of the Gaussian beam at the medium entrance $z = 0$. We will use Eqs. (91a)-(93) to study the interaction and propagation of the VV beam within the atomic medium. It should be noted that we defined the LG beams only at $z = 0$, since the interaction with the atomic medium alters the propagation behavior, making it different with the free-space propagation.

2 Work Methodology

2.1 Coherently prepared tripod scheme: model and equations derivation

2.1.1 The Hamiltonian of the tripod atom-field system

We consider a vectorial vortex (VV) beam constructed from a superposition of circularly polarized pulses with right- and left-handed polarizations, each carrying an opposite OAM charge of $+l\hbar$ and $-l\hbar$ respectively. The total electric field of this VV beam can be written as $\vec{E} = E_L\hat{e}_L + E_R\hat{e}_R$, where E_L and E_R are the slowly varying envelopes associated with the left- and right-circularly polarized unit vectors $\hat{e}_L$ and $\hat{e}_R$, respectively. The corresponding Rabi frequencies of the right- and left-circular components are denoted by Ω_R and Ω_L, and are related to the electric field through $\Omega_{R(L)} = \vec{Q}_{R(L)} \cdot \vec{E}_{R(L)}/\hbar$, where $\vec{Q}_{R(L)}$ represents the dipole moment of the atomic transition coupled to the electric-field component $\vec{E}_{R(L)}$ [36]. We also consider a third control field, $\vec{E}_C = E_C\vec{e}_C$ without OAM and polarization unit vector $\vec{e}_C$ that can be chosen arbitrarily. The Rabi frequency of this control field is $\Omega_C = \vec{Q}_C \cdot \vec{E}_C/\hbar$ [36] which is assumed to be stronger compared to the VV beam's right- and left-handed components such that $\Omega_C \gg \Omega_R, \Omega_L$. This stronger control field will be important in order to control the transparency windows and dispersion behavior experienced by the VV beam components near the resonance of the EIT medium, similar to how the control field shaped the transparency windows and dispersion of a weak probe field in Fig. 3.

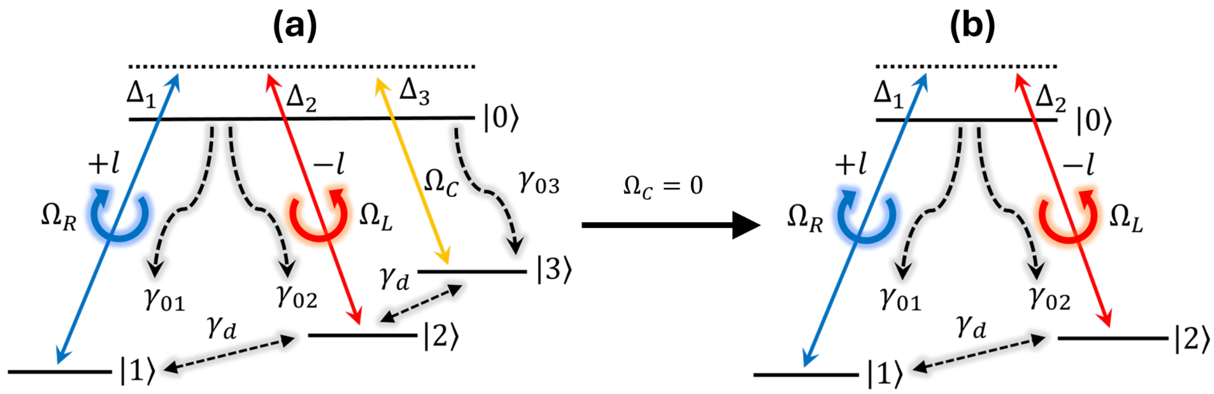

Figure 10: Schematic of the multi-level atom-light coupling. (a) Four-level atomic system forming a tripod configuration. The right- and left-handed circularly polarized light fields, with Rabi frequencies Ω_R and Ω_L, couple the $|1\rangle \to |0\rangle$ and $|0\rangle \to |2\rangle$ transitions, respectively, while the control light field, with Rabi frequency Ω_C, couples the $|0\rangle \to |3\rangle$ transition. (b) Three-level atomic system forming a Λ configuration in the absence of the control field.

For the model of the EIT medium, we consider a medium consisting of an identical ensemble of four-level atomic system where each of the atoms have three ground states $|1\rangle, |2\rangle, |3\rangle$ and one excited state $|0\rangle$. We assume the atomic ensemble is initially prepared in a coherent superposition between two of its ground state $|1\rangle$ and $|2\rangle$ before any interaction with the VV beam components and the control field which is also known as the phaseonium medium [36]. The initial wave function of the phaseonium can be written as:

$$|\psi(t=0)\rangle = \cos\theta\,|1\rangle + \sin\theta\,|2\rangle\,, \tag{94}$$

where θ is a tuning angle that describe the relative populations between $|1\rangle$ and $|2\rangle$. When the atom interacts with the laser fields, the VV beam components coupled the coherently prepared ground states $|1\rangle$ and $|2\rangle$ with the excited state $|0\rangle$, where the right-handed vortex component Ω_R drives the $|1\rangle \to |0\rangle$ transitions, while the left-handed vortex component drives the $|2\rangle \to |0\rangle$ transitions. The stronger control field Ω_C coupled the third unoccupied ground state $|3\rangle$ to the excited state $|0\rangle$, driving the $|3\rangle \to |0\rangle$ transitions. This interactions formed a tripod configurations illustrated in Fig. 10(a). When the control field is turned off, the configuration atom-light coupling scheme reduces to the Λ configuration illustrated in Fig. 10(b), which has been studied in our previous investigation [25]. The Hamiltonian of the tripod configuration can be expressed similarly to Eq. (47) under the *dipole approximation* and the *rotating wave approximation* as the following:

$$\hat{H}_{\text{Tripod}} = \hat{H}_{\text{Atom}} + \hat{H}_{\text{Atom-field}}, \tag{95a}$$

$$\hat{H}_{\text{Atom}} = \sum_{j=0}^{3} \hbar\omega_j\,|j\rangle\langle j|\,, \tag{95b}$$

$$\hat{H}_{\text{Atom-field}} = \hbar\Omega_R^* e^{-i\omega t}\,|0\rangle\langle 1| + \hbar\Omega_L^* e^{-i\omega t}\,|0\rangle\langle 2| + \hbar\Omega_C^* e^{-i\omega_C t}\,|0\rangle\langle 3| + \text{H.c.}, \tag{95c}$$

where ω is the optical frequency of the VV beam, ω_C is the optical frequency of the control field, while ω_j is the eigen-frequency of the atomic state $|j\rangle$ for $j = 0, 1, 2, 3$, while H.c. denotes the Hermitian conjugate of the atom-field Hamiltonian.

The Hamiltonian can be expressed in a time-independent form under the appropriate rotating-wave frame. To do that, we introduce the following unitary transformation:

$$\hat{W} = e^{i\omega_0 t|0\rangle\langle 0| + i(\omega_0-\omega)t|1\rangle\langle 1| + i(\omega_0-\omega)t|2\rangle\langle 2| + i(\omega_0-\omega_C)t|3\rangle\langle 3|}, \tag{96}$$

under which the Hamiltonian defined in Eqs. (95a)-(95c) transforms according to Eq. (48), and yields

$$\begin{aligned}\hat{H}'_{\text{Tripod}} =& -\hbar\Delta_1\,|1\rangle\langle 1| - \hbar\Delta_2\,|2\rangle\langle 2| - \hbar\Delta_3\,|3\rangle\langle 3| \\ &+ \hbar\Omega_R\,|1\rangle\langle 0| + \hbar\Omega_L\,|2\rangle\langle 0| + \hbar\Omega_C\,|3\rangle\langle 0| + H.c.,\end{aligned} \tag{97}$$

where the detunings of the optical fields are defined as

$$\Delta_1 = \omega_0 - \omega_1 - \omega, \tag{98a}$$

$$\Delta_2 = \omega_0 - \omega_2 - \omega, \tag{98b}$$

$$\Delta_3 = \omega_0 - \omega_3 - \omega_C. \tag{98c}$$

Before moving further, it is important to note that the coherent superposition of the ground states defined by Eq. (94) is possible to realized experimentally using stimulated Raman adiabatic passage (STIRAP) [49]. This technique allows population transfer between quantum states without being affected by the loss from stimulated emission. In practice, STIRAP is done by using two additional laser fields, namely the pump and Stokes fields. Typically, a counter-intuitive sequence of pulses is used, in which the Stokes laser is turned on first to couple the $|2\rangle \rightarrow |0\rangle$ transition, and after a controlled time-delay, the pump laser is turned on to create a small temporal overlap between the two pulses. By slowly increasing the pump-laser intensity and decreasing the Stokes-laser intensity, the population can be transferred adiabatically from $|2\rangle$ to $|1\rangle$ without populating the excited state $|0\rangle$. An example of medium for implementing the tripod atom-light configuration is a well-characterized atomic system, such as the system of ^{87}Rb atomic vapour, where the Zeeman sub-levels can be used to represent each of the four-level atomic bare states [32]. The coherently prepared ground-states $|1\rangle$ and $|2\rangle$ can be represented by the states $\left|5S_{1/2}, F = 1, m = -1\right\rangle$ and $\left|5S_{1/2}, F = 1, m = +1\right\rangle$, respectively. The third unoccupied ground-state $|3\rangle$ can be represented by $\left|5S_{1/2}, F = 2, m = \pm 1\right\rangle$, while the excited state $|0\rangle$ is represented by $\left|5P_{3/2}, F = 1, m = 0\right\rangle$. Since the third unoccupied ground-state belongs to a different hyperfine manifold ($F = 2, m_f = \pm 1$), from the phaseonium states ($F = 1, m_f = \pm 1$), the choice of the polarization for the control field can be chosen arbitrarily between right- or left-handed circular polarization.

2.1.2 Bloch equations and the steady state solutions of the tripod configuration

We study the dynamics of the atomic density matrix using the LVNE in Eq. (26). In contrast to our previous study of the Λ configuration in [25] where the system was assumed to relax solely via spontaneous emission, we also consider the effect of non-radiative relaxation, which introduces dephasing of coherence between the ground-states $|1\rangle$, $|2\rangle$, and $|3\rangle$. We follow a similar approach described in [22], in which the non-radiative relaxation is assumed to be caused by collisions between ground states. In this approach, a new relaxation term, $\hat{\mathcal{L}}$, is included in the LVNE in Eq. (26) as follows:

$$\dot{\hat{\rho}} = -\frac{i}{\hbar}\left[\hat{H}, \hat{\rho}\right] - \hat{\mathcal{L}}, \tag{99}$$

where $\hat{\mathcal{L}}$ is defined as the following [22]:

$$\hat{\mathcal{L}} = \hat{\mathcal{L}}_r + \hat{\mathcal{L}}_c, \tag{100a}$$

$$\hat{\mathcal{L}}_r = \sum_{j=1}^{3} \frac{\gamma_{0j}}{2} \left(|0\rangle\langle 0| \rho - |j\rangle\langle j| \rho_{00} + \rho |0\rangle\langle 0|\right), \tag{100b}$$

$$\hat{\mathcal{L}}_c = \sum_{j=1}^{3} \sum_{j \neq i=1}^{3} \frac{\gamma_d}{2} \left(|j\rangle\langle j| \rho - 2|i\rangle\langle i| \rho_{jj} + \rho |j\rangle\langle j|\right). \tag{100c}$$

The term $\hat{\mathcal{L}}_r$ describes the radiative relaxation from the excited state $|0\rangle$ to the ground state $|j\rangle$ caused by spontaneous emission, with decay rates γ_{0j} ($j = 1, 2, 3$). The term $\hat{\mathcal{L}}_c$ describes the non-radiative relaxation caused by the collisions between ground states, leading to dephasing of the ground-state coherences ρ_{ij} ($i, j = 1, 2, 3$) with the dephasing rate γ_d. Here, γ_d can be assumed to be negligible compared with the radiative decay rate γ_{0j} in cold atomic systems [22]. By substituting the time-independent Hamiltonian in Eq. (97) and the relaxation terms in Eqs. (100a)-(100c), we obtained the following set of optical Bloch equations for the coherences:

$$\dot{\rho}_{11} = i(\Omega_R^*\rho_{14} - \Omega_R\rho_{01}) + \gamma_{01}\rho_{00} + \gamma_d(\rho_{22} + \rho_{33} - 2\rho_{11}), \tag{101a}$$

$$\dot{\rho}_{22} = i(\Omega_L^*\rho_{20} - \Omega_L\rho_{02}) + \gamma_{02}\rho_{00} + \gamma_d(\rho_{11} + \rho_{33} - 2\rho_{22}), \tag{101b}$$

$$\dot{\rho}_{33} = i(\Omega_C^*\rho_{30} - \Omega_C\rho_{03}) + \gamma_{03}\rho_{00} + \gamma_d(\rho_{11} + \rho_{22} - 2\rho_{33}), \tag{101c}$$

$$\dot{\rho}_{12} = i(\rho_{12}(\Delta_1 - \Delta_2) + \Omega_L^*\rho_{10} - \Omega_R\rho_{01}) - 2\gamma_d\rho_{12}, \tag{101d}$$

$$\dot{\rho}_{13} = i(\rho_{13}(\Delta_1 - \Delta_3) + \Omega_C^*\rho_{10} - \Omega_R\rho_{03}) - 2\gamma_d\rho_{13}, \tag{101e}$$

$$\dot{\rho}_{10} = i(\Omega_R\rho_{11} + \Omega_L\rho_{12} + \Omega_C\rho_{13} + \Delta_1\rho_{10}) - i\Omega_R\rho_{00} - \Gamma\rho_{10} - \gamma_d\rho_{10}, \tag{101f}$$

$$\dot{\rho}_{23} = i(\rho_{23}(\Delta_2 - \Delta_3) + \Omega_C^*\rho_{20} - \Omega_L\rho_{03}) - 2\gamma_d\rho_{23}, \tag{101g}$$

$$\dot{\rho}_{20} = i(\Omega_R\rho_{21} + \Omega_L\rho_{22} + \Omega_C\rho_{23} + \Delta_2\rho_{20}) - i\Omega_L\rho_{00} - \Gamma\rho_{20} - \gamma_d\rho_{20}, \tag{101h}$$

$$\dot{\rho}_{30} = i(\Omega_R\rho_{31} + \Omega_L\rho_{32} + \Omega_C\rho_{33} + \Delta_3\rho_{30}) - i\Omega_C\rho_{00} - \Gamma\rho_{30} - \gamma_d\rho_{30}, \tag{101i}$$

where we have defined the parameter Γ as

$$\Gamma = \frac{\gamma_{01} + \gamma_{02} + \gamma_{03}}{2}. \tag{102}$$

Since the Hamiltonian is a 4×4 matrix constructed in the orthonormal basis of the four-level atomic states, the total number of coupled optical Bloch equations is 16, corresponding to all density matrix elements ρ_{ij} with $i, j = 0, 1, 2, 3$. However, nine equations obtained in Eqs. (101a)-(101i) are sufficient to describe the dynamics of the system, since the remaining optical Bloch equations can be obtained from the Hermitian property of the density matrix, $\rho_{ij} = \rho_{ji}^*$, and the conservation of probability, $\sum_{j=0}^{3}\rho_{jj} = 1$.

In our case of interest, we assume that the right- and left-handed vortex components are weakly interacting with the atomic medium, such that the system satisfies the weak probe limit $|\Omega_R|, |\Omega_L| \ll |\Omega_C|$. Within this weak probes limit, the solution for the coherences can be obtained in the steady-state regime using a perturbative expansion of the density matrix elements with respect to the probe fields. The perturbative expansion is written as the following:

$$\Omega_R \to \beta\Omega_R, \tag{103a}$$

$$\Omega_L \to \beta\Omega_L, \tag{103b}$$

$$\rho_{ij} \to \rho_{ij}^{(0)} + \beta\rho_{ij}^{(1)} + \beta^2\rho_{ij}^{(2)} + \beta^3\rho_{ij}^{(3)} + \cdots, \tag{103c}$$

where β denotes a small constant of perturbation with $\beta \ll 1$, while $\rho_{ij}^{(0)}, \rho_{ij}^{(1)}, \rho_{ij}^{(2)}$, and $\rho_{ij}^{(3)}$ respectively are the zeroth-, first-, second-, and third-order expansion terms of ρ_{ij} in the probe fields Ω_R and Ω_L for the $|i\rangle \to |j\rangle$ transition, respectively. This expansion allows us to study the linear as well as nonlinear response of the medium to the probe fields. The relations between the linear susceptibilities, $\chi^{(1)}$, and the first order coherence terms, $\rho_{ij}^{(1)}$, can be obtained by substituting Eq. (103c) into Eq. (64). However a condition should be imposed where the zeroth-order terms for the ground state populations satisfy the probability conservation condition $\sum_{j=1}^{3}\rho_{jj}^{(0)} = 1$, while the excited-state population $\rho_{00}^{(0)}$ and the remaining zeroth-order coherences $\rho_{ij}^{(0)}$ are zero. This is due to the probe fields are too weak to drive the transition from the ground to the excited state in the weak-probe limit. This condition, together with the phaseonium state defined in Eq. (94), yields the zeroth-order coherences as the following:

$$\rho_{00}^{(0)} = \rho_{33}^{(0)} \approx 0, \tag{104a}$$
$$\rho_{11}^{(0)} \approx \cos^2(\theta), \tag{104b}$$
$$\rho_{22}^{(0)} \approx \sin^2(\theta), \tag{104c}$$
$$\rho_{12}^{(0)} = \rho_{21}^{(0)} \approx \sin(\theta)\cos(\theta), \tag{104d}$$

while the remaining zeroth order terms are zero.

The first order coherences can be obtained in the steady state regime by substituting the expansion in Eqs. (103a)- (103c) into Eqs. (101a)-(101i) and setting the time-derivative on the left-hand side of each equations to zero, $\dot{\rho}_{ij} = 0$, for $i, j = 0, 1, 2, 3$. However, it is not necessary to work with all nine equations, since we only need the solutions for $\rho_{10}^{(1)}$ and $\rho_{20}^{(1)}$, which are the coherences related to the transitions driven by the Ω_R and Ω_L respectively. The following set of coupled equations is then obtained:

$$\rho_{10}^{(1)} = \frac{\Omega_R(\rho_{00}^{(0)} - \rho_{11}^{(0)}) - \Omega_L\rho_{12}^{(0)}}{\Delta_1 + i(\Gamma + \gamma_d)} - \frac{\Omega_C\rho_{13}^{(1)}}{\Delta_1 + i(\Gamma + \gamma_d)}, \tag{105a}$$
$$\rho_{20}^{(1)} = \frac{\Omega_L(\rho_{00}^{(0)} - \rho_{22}^{(0)}) - \Omega_R\rho_{21}^{(0)}}{\Delta_2 + i(\Gamma + \gamma_d)} - \frac{\Omega_C\rho_{23}^{(1)}}{\Delta_2 + i(\Gamma + \gamma_d)}, \tag{105b}$$

$$\rho_{13}^{(1)} = \frac{\Omega_R\rho_{03}^{(0)} - \Omega_C^*\rho_{10}^{(1)}}{\Delta_1 - \Delta_3 + 2i\gamma_d}, \tag{105c}$$
$$\rho_{23}^{(1)} = \frac{\Omega_L\rho_{03}^{(0)} - \Omega_C^*\rho_{20}^{(1)}}{\Delta_2 - \Delta_3 + 2i\gamma_d}. \tag{105d}$$

Equations (105a)-(105d) can be solved together with the zeroth-order terms obtained in Eqs. (104a)-(104d). This yields the following solutions of the probe-driven transitions:

$$\rho_{10}^{(1)} = -\frac{\Omega_R\cos^2(\theta) + \Omega_L\sin(\theta)\cos(\theta)}{\Delta_1 - \frac{|\Omega_C|^2}{\Delta_1 - \Delta_3 + 2i\gamma_d} + i(\Gamma + \gamma_d)}, \tag{106a}$$
$$\rho_{20}^{(1)} = -\frac{\Omega_R\sin(\theta)\cos(\theta) + \Omega_L\sin^2(\theta)}{\Delta_2 - \frac{|\Omega_C|^2}{\Delta_2 - \Delta_3 + 2i\gamma_d} + i(\Gamma + \gamma_d)}. \tag{106b}$$

It is straightforward to verify that the behavior of the tripod atom-field configuration reduces to that of the Λ configuration without the presence of the control field. When the control field is turned off, $|\Omega_C| = 0$, Eqs. (106a) and (106b) reduce into:

$$\rho^{(1)}_{10,\Lambda} = -\frac{\Omega_R \cos^2(\theta) + \Omega_L \sin(\theta)\cos(\theta)}{\Delta_1 + i(\Gamma + \gamma_d)}, \tag{107a}$$

$$\rho^{(1)}_{20,\Lambda} = -\frac{\Omega_R \sin(\theta)\cos(\theta) + \Omega_L \sin^2(\theta)}{\Delta_2 + i(\Gamma + \gamma_d)}, \tag{107b}$$

which are the solutions for the atomic coherence of the Λ configuration in our previous work [25] in the limit $\gamma_d \to 0$.

The validity of the first-order approximation requires $|\rho_{10}|, |\rho_{20}| \ll 1$. Outside this regime, particularly in the strong-coupling limit, the ground-state populations ρ_{11} and ρ_{22} can change during propagation with non-negligible evolution. In the weak-probe regime considered in this work, however, the excited-state population ρ_{00} is absent at first order in the perturbative expansion. Its contribution appears only at second and higher orders, where it gives rise to optical pumping and, consequently, depletes the initially prepared ground-state coherence defined in Eq. (94). Under such conditions, the population excited by the probe does not completely return to the original coherent superposition, but instead undergoes incoherent decay.

These higher-order contributions become important only in the nonlinear regime, where the probe intensities are no longer negligible. By contrast, if the analysis is restricted to the linear regime, the weak-probe condition ensures that the initially prepared coherence remains essentially unchanged throughout propagation. In addition, the probe fields and control field are treated as pulses with finite temporal duration rather than as continuous waves. Provided that the pulse duration is longer than the optical coherence formation time, which is determined by the spontaneous decay rate, the atomic response remains in the quasi-steady-state regime and the prepared ground-state coherence is maintained. For example, in ^{87}Rb vapor, a typical decay rate is $\gamma \sim 2\pi \times 6$ MHz, corresponding to a lifetime of approximately 100 ns. Therefore, probe pulses with durations longer than 100 ns, which are commercially available, allow the atoms to adiabatically follow the instantaneous steady-state optical coherence.

2.1.3 Propagation equations of optical vector vortices and their solutions in the tripod atomic configuration

The propagation of the vector vortices inside the tripod atomic medium in the linear regime can be studied using the MBE defined in Eq. (83). Multiplying both sides of Eq. (83) by $\frac{Q_{0j}}{\hbar}$ and using the relation between polarization density $\mathcal{P}_0$ and the density-matrix elements ρ_{0j} corresponding to the transitions driven by the probe field Ω_k, we obtained:

$$\frac{\partial \Omega_k}{\partial z} + \frac{1}{c}\frac{\partial \Omega_k}{\partial t} = \frac{ikN|Q_{0j}|^2}{2\varepsilon_0 \hbar}\rho_{j0}. \tag{108}$$

We can rewrite the term on the right-hand side of Eq. (108) in terms of the spontaneous-emission decay rate γ_{0j} from the excited state $|0\rangle$ to the ground state $|j\rangle$, which is related to the parameter Γ defined in Eq. (102). We use the following relation between γ_{0j} and $|Q_{0j}|$, obtained from the

Fermi's golden rule [50]:

$$\gamma_{0j} = \frac{\omega_{0j}^3 |Q_{0j}|^2}{3\pi\varepsilon_0 \hbar c^3}, \tag{109}$$

where ω_{0j} is the emission frequency related to the $|0\rangle \to |j\rangle$ transition. Assuming that the decay rates for the transitions from the excited state $|0\rangle$ to each of the ground states $|1\rangle$, $|2\rangle$, and $|3\rangle$ are equal ($\gamma_{01} = \gamma_{02} = \gamma_{03} = \gamma$), and using Eq. (109), we can rewrite Eq. (108) as:

$$\frac{\partial \Omega_k}{\partial z} + \frac{1}{c}\frac{\partial \Omega_k}{\partial t} = i\zeta\Gamma\rho_{j0}, \tag{110}$$

where the constant ζ satisfies:

$$\zeta = \frac{\pi N c^2}{\omega^2}. \tag{111}$$

Thus, the evolution of the right- and left-handed vortex fields, Ω_R and Ω_L, respectively, can be described by the following MBEs:

$$\frac{\partial \Omega_R}{\partial z} + \frac{1}{c}\frac{\partial \Omega_R}{\partial t} = i\zeta\Gamma\rho_{10}, \tag{112a}$$
$$\frac{\partial \Omega_L}{\partial z} + \frac{1}{c}\frac{\partial \Omega_L}{\partial t} = i\zeta\Gamma\rho_{20}, \tag{112b}$$

where the two equations are indirectly coupled via the atomic coherences ρ_{01} and ρ_{02}, which depend on both the right- and left-handed vortex components from the solutions obtained in Eqs. (106a)-(106b). The transverse derivative term, which corresponds to the effect of diffraction, is neglected in Eqs. (112a)-(112b), assuming that the propagation distance inside the atomic medium is sufficiently small. Under this assumption, the phase change induced by the transverse evolution is small compared to the longitudinal evolution. The transverse evolution can be estimated as $\nabla_\perp^2 \Omega_k \sim w^{-2}\Omega_k$, where w denotes the beam waist of a Gaussian beam. The phase shift caused by diffraction can be estimated as $\frac{L}{2kw^2}$, where $k = \frac{2\pi}{\lambda}$ is the wave number of the beam and L is the propagation distance inside the medium. The effect of the diffraction can be neglected if the total phase shift is much lower than π. Therefore, the condition under which diffraction can be neglected is $\frac{L\lambda}{w^2} \ll \pi$. Since the optical properties such as the wavelength and beam waist are fixed during the experiment, the diffraction-free condition can be satisfied by choosing an appropriate medium length L.

For simplification, the vortex fields are assumed to have equal detunings, $\Delta_1 = \Delta_2 = \Delta$. Under this assumption, Eqs. (112a)-(112b) can be combined in the steady-state regime, such that the evolution of the vortex fields is described by:

$$\frac{\partial}{\partial z}\begin{bmatrix}\Omega_R \\ \Omega_L\end{bmatrix} = -iK\begin{bmatrix}\Omega_R \\ \Omega_L\end{bmatrix}, \tag{113}$$

where K is a matrix defined by

$$K = Q\begin{bmatrix}\cos^2(\theta) & \sin(\theta)\cos(\theta) \\ \sin(\theta)\cos(\theta) & \sin^2(\theta)\end{bmatrix}, \tag{114}$$

with Q satisfying

$$Q = \zeta\Gamma \frac{1}{\Delta - \frac{|\Omega_C|^2}{\Delta - \Delta_C + 2i\gamma_d} + i(\Gamma + \gamma_d)}, \tag{115}$$

which depends on the atomic parameters through the constant ζ, the two-photon detuning Δ, the control field detuning Δ_3, the parameter Γ related to the radiative decay rate, and the non-radiative dephasing rate γ_d.

The solutions of Eqs. (113)-(115) can be determined by setting an initial conditions at the medium entrance, $z = 0$, such that $\Omega_R(0) = \Omega_{R,0}$ and $\Omega_L(0) = \Omega_{L,0}$. The corresponding solutions for the Rabi frequencies $\Omega_R(z)$ and $\Omega_L(z)$ along the propagation direction are then given by

$$\Omega_R(z) = \Omega_{R,0}\left(\sin^2(\theta) + \cos^2(\theta)e^{-iQz}\right) + \Omega_{L,0}\sin(\theta)\cos(\theta)\left(e^{-iQz} - 1\right), \tag{116a}$$

$$\Omega_L(z) = \Omega_{R,0}\sin(\theta)\cos(\theta)\left(e^{-iQz} - 1\right) + \Omega_{L,0}\left(\cos^2(\theta) + \sin^2(\theta)e^{-iQz}\right), \tag{116b}$$

where $\Omega_{R,0}$ and $\Omega_{L,0}$ are the Rabi amplitudes of the initial vortex fields at the medium entrance. These amplitudes are related to the initial electric fields of the right- and left-handed vortex components defined in Eqs. (91a)-(91c). Explicitly, by multiplying both vortex-field components in Eqs. (91a)-(91c) with $Q_{0j}/\hbar$, we can rewrite Eqs. (91a)-(93) in terms of the initial Rabi frequencies $\Omega_{R,0}$ and $\Omega_{L,0}$ as the follows:

$$\vec{\Omega}(r, \phi, z = 0) = \Omega_{R,0}(r, \phi)\vec{e}_R + \Omega_{L,0}(r, \phi)\vec{e}_L, \tag{117a}$$

$$\Omega_{L,0} = \varepsilon\cos\alpha\left(\frac{r}{w_0}\right)^{|l|} e^{-\frac{r^2}{w^2}} e^{-il\phi}, \tag{117b}$$

$$\Omega_{R,0} = \varepsilon e^{i\varphi}\sin\alpha\left(\frac{r}{w_0}\right)^{|l|} e^{-\frac{r^2}{w^2}} e^{il\phi}. \tag{117c}$$

Equations (116a)-(117c) altogether will be used together to describe the evolution of the intensity and polarization state of the vector vortex beam throughout the propagation inside the tripod atomic medium. A detailed discussion about these evolutions is provided in Section 3.

2.1.4 Optical susceptibilities of the tripod atom-field system

The linear and nonlinear susceptibilities are directly related to the coherences of the atomic transitions driven by the vortex components. In the linear and nonlinear regimes, these relations are given by [11]:

$$\chi_k^{(1)} \approx \frac{N|Q_{ij}|^2}{\varepsilon_0\hbar\Omega_k}\rho_{ji}^{(1)}, \tag{118a}$$

$$\chi_k^{(3)} \approx \frac{N|Q_{ij}|^4}{\varepsilon_0\hbar\Omega_k^3}\rho_{ji}^{(3)}, \tag{118b}$$

where $\chi_k^{(n)}$ denotes the $n-$th order susceptibility, which is related to the $n-$th order coherence $\rho_{ij}^{(k)}$ corresponding to the $|j\rangle \rightarrow |i\rangle$ transition driven by the probe field Ω_k. However, we will limit the scope of this study to the linear response of the medium. Thus, in this section, we focus only on the relation between the linear susceptibility and the first-order coherences. We can rewrite the definition of the linear susceptibility in Eq. (118a) in terms of the spontaneous-emission decay rate γ_{0j} from the excited state $|0\rangle$ to the ground state $|j\rangle$, which is related to the parameter Γ defined in Eq. (102). Using the relation between γ_{0j} and $|Q_{0j}|$ obtained from Fermi's golden rule in Eq. (109), we can rewrite Eq. (118a) into:

$$\chi_k^{(1)} \approx \frac{3\pi N c^3 \gamma_{0j}}{\omega_{0j}^3 \Omega_k} \rho_{j0}^{(1)}. \tag{119}$$

Using the definition of Γ in Eq. (102) and following the same assumption of equal spontaneous emission decay rates, the linear susceptibility then become:

$$\chi_k^{(1)} \approx \frac{2\pi N c^3 \Gamma}{\omega_{0j}^3 \Omega_k} \rho_{j0}^{(1)}. \tag{120}$$

The linear susceptibilities experienced by the right- and left-handed vortex components in the tripod atomic configuration can be obtained by combining Eq. (120) with Eqs. (106a)-(106b). This yields:

$$\chi_R^{(1)} = \frac{2\zeta c\Gamma}{\omega} \frac{\cos^2(\theta) + \frac{\Omega_L}{\Omega_R}\sin(\theta)\cos(\theta)}{\Delta - \frac{|\Omega_C|^2}{\Delta - \Delta_3 + 2i\gamma_d} + i(\Gamma + \gamma_d)}, \tag{121a}$$

$$\chi_L^{(1)} = \frac{2\zeta c\Gamma}{\omega} \frac{\frac{\Omega_R}{\Omega_L}\sin(\theta)\cos(\theta) + \sin^2(\theta)}{\Delta - \frac{|\Omega_C|^2}{\Delta - \Delta_3 + 2i\gamma_d} + i(\Gamma + \gamma_d)}, \tag{121b}$$

where the emission frequency ω_{0j} is assumed to be approximately equal to the optical frequency of the vortex beam, ω. It should be noted that Ω_R and Ω_L in Eqs. (121a)-(121b) are position-dependent and satisfy the propagating-field solutions obtained in Eqs. (116a)-(116b). In general, Eqs. (121a) and (121b) reveal an anisotropic medium response to the different polarizations component of the vector vortex beam. The susceptibilities depend on the atomic coherence through the population tuning angle θ and on the OAM charge l of the vortex beam through the ratio of the field-amplitudes $\frac{\Omega_R}{\Omega_L}\left(\frac{\Omega_L}{\Omega_R}\right)$, which are not identical for χ_R and χ_L. The effect of this anisotropy on the beam evolution will be discussed in detail in Section3.

2.2 Stokes parameters for polarization characterization

The states of polarization in two-dimension can be illustrated using a polarization ellipse which describes how the electric field components in the transverse plane oscillate. Assuming that the wave propagate in z direction while the transverse plane is in the $x-y$ plane, the electric field components can be written in cartesian basis as:

$$\vec{E} = a_x\vec{e}_x + a_y\vec{e}_y, \tag{122}$$

where a_x and a_y respectively are the electric field amplitudes in the x and y directions. The polarization ellipse that corresponds to the direction of oscillation for the field in Eq. (105) is given in Fig. 11 where M_i and M_a respectively denotes the orientation of the minor and major axes of the ellipse, while ζ and ξ respectively denote the ellipticiy and the orientation of the ellipse. Three distinct state of polarization can be described by the ellipticity: $\zeta = 0$ for linear polarization, $\zeta = \pm\frac{\pi}{4}$ for the circular polarizations, and $0 < |\zeta| < \pi/4$ for the elliptical polarization [51].

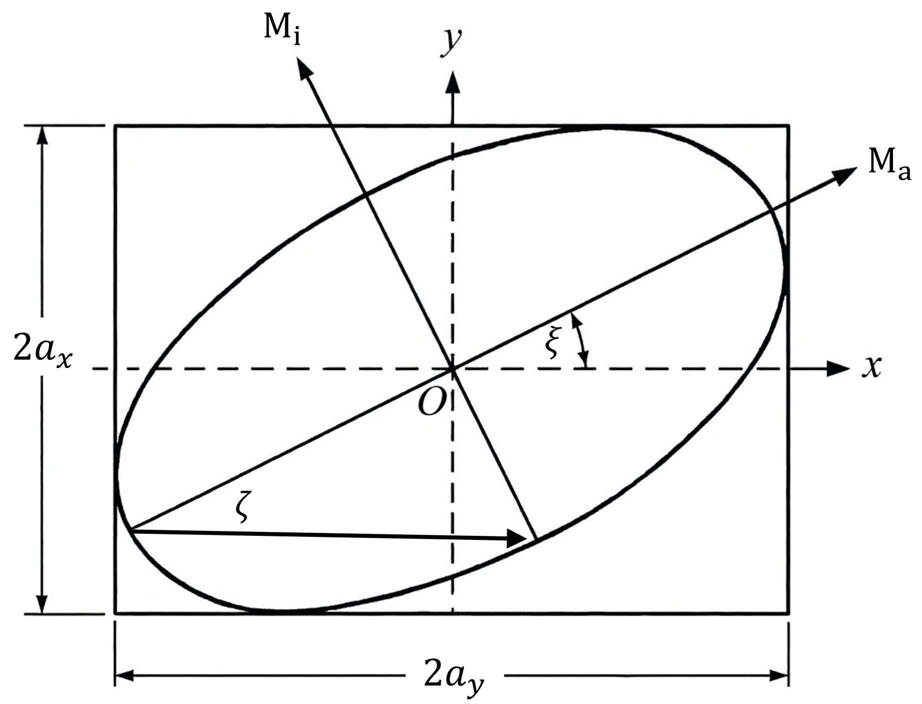

Figure 11: Polarization ellipse in the cartesian basis. Here ζ denotes the ellipticity, and ξ denotes the ellipse major axis orientation with respect to the cartesian x axis [51].

To characterize the polarization ellipse, we introduce the Stokes parameters. The stokes parameters in cartesian basis are defined as [51]:

$$S_0 = |a_x|^2 + |a_y|^2, \tag{123a}$$

$$S_1 = |a_x|^2 - |a_y|^2, \tag{123b}$$

$$S_2 = 2\mathrm{Re}(E_x E_y^*), \tag{123c}$$

$$S_3 = 2\mathrm{Im}(E_x E_y^*), \tag{123d}$$

where S_0 denotes the beam intensity, while S_1, S_2, and S_3 are related to the ellipticity and ellipse orientation. The relations are given by [51]:

$$S_1 = S_0 \cos(2\zeta) \sin(2\xi), \tag{124a}$$

$$S_2 = S_0 \cos(2\zeta) \cos(2\xi), \tag{124b}$$

$$S_3 = S_0 \sin(2\zeta). \tag{124c}$$

Moreover, it is also possible to transform the Stokes parameters in cartesian basis into circular polarization basis. Using the following relation between the circular polarization and cartesian basis:

$$\vec{e}_R = \frac{1}{\sqrt{2}}\left(\vec{e}_x - i\vec{e}_y\right), \quad \vec{e}_L = \frac{1}{\sqrt{2}}\left(\vec{e}_x + i\vec{e}_y\right), \tag{125}$$

the Stokes parameters in Eqs. (123a)-(123d) can be re-written in the circular polarization basis as [19]:

$$S_0 = |E_R|^2 + |E_L|^2, \tag{126a}$$

$$S_1 = 2\mathrm{Re}(E_R^* E_L), \tag{126b}$$

$$S_2 = 2\mathrm{Im}(E_R^* E_L), \tag{126c}$$

$$S_3 = |E_R|^2 - |E_L|^2. \tag{126d}$$

This basis of the Stokes vectors will be used to characterize the SOP dynamics for the VV beam throughout our investigation.

3 Results and Discussion

3.1 Absorption and dispersion properties of the tripod atomic configuration

3.1.1 Absorption and dispersion profile

The linear absorption properties of the medium experienced by the right- and left-handed vortex are determined from the imaginary part of the susceptibilities, $\mathrm{Im}\left[\chi_R^{(1)}\right]$ and $\mathrm{Im}\left[\chi_L^{(1)}\right]$, whereas the dispersion properties are determined from the real part $\mathrm{Re}\left[\chi_R^{(1)}\right]$ and $\mathrm{Re}\left[\chi_L^{(1)}\right]$. From this point, we assumed that the non-radiative dephasing rate γ_d is much smaller than the radiative decay rate Γ, where we choose $\gamma_d = 10^{-3}\Gamma$. This choice of dephasing rate order of magnitude is within a valid range reported in [22] and [52], assuming that the considered atomic media is a cold atomic system. To further simplify the discussion in this section, we first consider the case where both of the phaseonium ground states $|1\rangle$ and $|2\rangle$ are equally populated. This is done by setting the coherence tuning angle $\theta = \pi/4$. We also consider the case where the initial amplitudes at the medium entrance $z = 0$ of the right- and left-handed components are equal and without relative phase difference by setting $\alpha = \pi/4$ and $\varphi = 0$ respectively. Under these considerations, the propagating field solutions in Eqs. (116a)-(117c) simplify into:

$$\Omega_R(z) = \varepsilon A(r)\left(e^{-iQz}\cos(l\phi) + i\sin(l\phi)\right), \tag{127a}$$

$$\Omega_L(z) = \varepsilon A(r)\left(e^{-iQz}\cos(l\phi) - i\sin(l\phi)\right), \tag{127b}$$

where $A(r)$ is the radial function defined in Eq. (93). The susceptibilities under the same condition also reduce to:

$$\chi_R^{(1)} = \frac{2c}{\omega}Q\frac{e^{-iQz}}{e^{-iQz} + i\tan(l\phi)} \tag{128a}$$

$$\chi_L^{(1)} = \frac{2c}{\omega}Q\frac{e^{-iQz}}{e^{-iQz} - i\tan(l\phi)}. \tag{128b}$$

It is clear that from Eqs. (128a) and (128b) that the susceptibilities are polarization dependent, which lead to a polarization dependent absorption and dispersion characteristics. As the absorption and dispersion are polarization dependent, the different components of the vector vortex beam will experience different attenuation and group delay during the propagation inside the atomic medium. This polarization dependent medium response originates from the coherent superposition of the phaseonium ground states $|1\rangle$ and $|2\rangle$ defined in Eq. (94), that introduce an effective anisotropy, even in the absence of the control field. This effective anisotropy also modify the absorption pattern, creating an azimuthally dependent transparency windows with $2|l|$ degeneracy at resonance $\Delta = 0$ when the control field is absent, which is also shown in our previous work [25]. When a nonzero control field is present in the system, the absorption is suppressed uniformly across the whole transverse plane at the resonance $\Delta = 0$, allowing the beam propagate with lower attenuation. The presence of the control field also modify the dispersion profile, where a positive slope of dispersion exist near the resonance $\Delta \approx 0$, leading to slow-light propagation of the vector vortex beam.

Figure 12 illustrate the absorption and dispersion behavior at the medium entrance $z = 0$ of the vector vortex beam with $|l| = 1$ in the presence of the control field. In this case, we assumed that the control field is on the resonance with $|1\rangle \longrightarrow |0\rangle$ transition such that $\Delta_3 = 0$, such that the absorption and dispersion behavior mainly depend on the normalized two-photon detuning Δ/Γ. Panels (a) and (b) depict the absorption profiles of the right- and left-handed components, respectively. The corresponding dispersion behavior is shown in panels (c) and (d) for the right-handed component, and in panels (e) and (f) for the left-handed component. The control field amplitude is fixed at $|\Omega_C| = \Gamma$. All quantities are normalized by $\frac{2c}{\omega}\zeta\Gamma$ such that the results can generalized to any cold atomic media.

As illustrated in all subfigures of Fig. 12 that both the absorption and dispersion exhibit a phase dependency with azimuthally (ϕ) varying profile. This phase-dependent behavior originates from the ratio of the $i\tan(l\phi)$ term in the susceptibility of the right-handed component and the $-i\tan(l\phi)$ term in the left-handed component as shown in Eqs. (128a) and (128b). These terms lead to an absorption and a dispersion profiles which vary periodically with the azimuthal angle ϕ, where the periodicity is $\frac{\pi}{|l|}$. For instance, in Fig. 12 where $|l| = 1$ is considered, the periodicity is π which can be seen in subplots (a)–(d), where the absorption and dispersion profiles of both the right- and left-handed components repeat for every integer multiples of $\phi = \pi$.

The profile of the imaginary parts of $\chi_R^{(1)}$ and $\chi_L^{(1)}$ do not only reveal the pattern of the absorption and the transparency, but a small gain region as well. From subfigures (a) and (b) in Fig. 12, it can be seen that near resonance ($\Delta/\Gamma = 0$), both the right- and left-handed components experience zero absorption as indicated by the blue color corresponding to $\mathrm{Im}[\chi_{R(L)}^{(1)}] = 0$ indicating a formation of a perfect EIT across the entire azimuthal plane. For the region shifted from exact resonance with nonzero detuning $\Delta/\Gamma \neq 0$, the response becomes azimuthally modulated. Two absorption peaks are observed around $|\Delta| = \Gamma$, shown in red that corresponds to $\mathrm{Im}[\chi_{R(L)}^{(1)}] > 0$. This absorption peaks indicate a strong attenuation at specific angular positions. Additionally, small gain regions are observed and represented by darker blue areas where $\mathrm{Im}[\chi_{R(L)}^{(1)}] < 0$.

The dispersion profiles of the right- and left-handed components can be seen in Fig. 12(c) and Fig. 12(e) respectively. In the region near the resonance ($|\Delta| < 0.5\Gamma$), the real part of susceptibility shows a transition from negative to positive values as the detuning increases. This transition corresponds to a positive slope of dispersion around $\Delta/\Gamma = 0$ that implies a slow-light propagation [11]. This positive slope of dispersion becomes clearer in the one-dimensional dispersion profiles shown in Fig. 12(d) for $\mathrm{Re}[\chi_R^{(1)}]$ and Fig. 12(f) for $\mathrm{Re}[\chi_L^{(1)}]$, for specific samples of azimuthal angle. It can be seen from the one-dimensional plots that for most values of ϕ, both circular polarization components exhibit a positive dispersion slope at resonance which is indicated by the vertical dashed lines at $\Delta/\Gamma = 0$. This implies the effect of slow-light propagation dominates across the transverse plane for both components, except at the specific angles of $\phi = \pi/2$ and $\phi = 3\pi/2$ where the slope of dispersion vanishes which corresponds to a local maxima or minima in the dispersion profile. However, these specific angles also correspond to the peak of absorption in the transverse plane where the intensity will be attenuated strongly and vanish as the beam propagate deeper through the

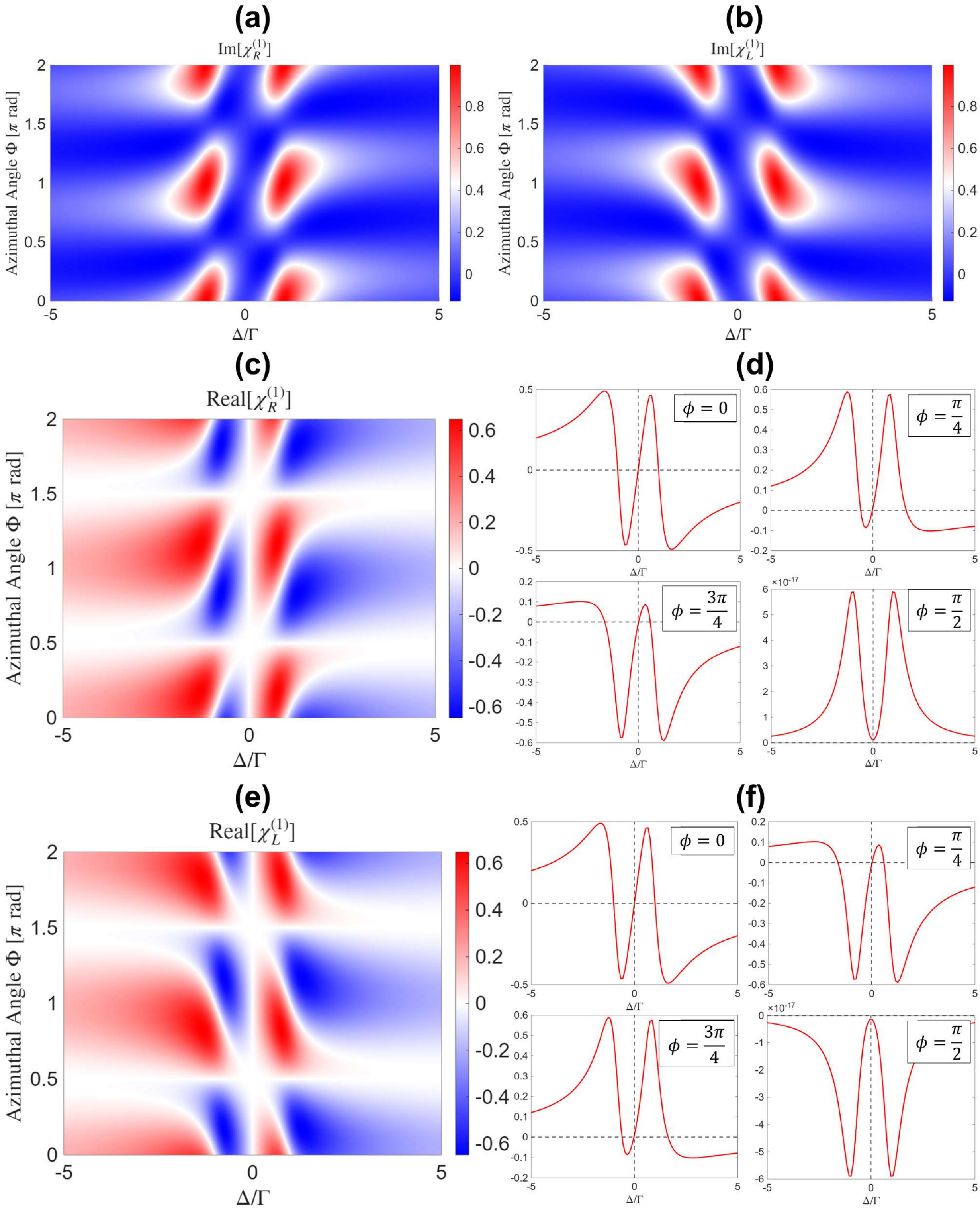

Figure 12: Absorption ($\mathrm{Im}[\chi^{(1)}]$) (a)–(b) and dispersion ($\mathrm{Re}[\chi^{(1)}]$) (c)–(f) profiles for the right- and left-handed components of the vector vortex beam with topological charge $|l| = 1$ at $z = 0$. Panels (a) and (b) show the imaginary part of the susceptibilities evaluated at $r = w$ as functions of azimuthal angle ϕ and detuning Δ/Γ for the right- and left-handed components, respectively. Panels (c) and (e) present the corresponding real parts. Panels (d) and (f) display the one-dimensional dispersion profiles, $\mathrm{Re}[\chi_R^{(1)}]$ and $\mathrm{Re}[\chi_L^{(1)}]$, plotted versus Δ/Γ for selected azimuthal angles $\phi = 0, \pi/4, \pi/2, 3\pi/4$. In (d) and (f), vertical dashed lines indicate resonance ($\Delta/\Gamma = 0$), while horizontal dashed lines denote $\mathrm{Re}[\chi_{R(L)}^{(1)}] = 0$. The parameters used are $\gamma_d = 10^{-3}\Gamma$, $|\Omega_C| = \Gamma$, $\theta = \pi/4$, $\alpha = \pi/4$, and $\varphi = 0$. All plots are normalized to $\frac{2c}{\omega}\zeta\Gamma$.

medium. Nevertheless, except at these isolated angles, the vector vortex beam propagates mainly in the slow-light regime because the control field establishes an EIT window. This reduced slow-light propagation behavior is absent in previous studies of vector vortices in EIT systems where the strong control field is absent [21, 22, 24, 25].

3.1.2 Reduced group velocity

In order to provide a more intuitive description of slow-light propagation, it is more natural to compute the group velocity of the vector vortex beam inside the medium. The exact expression for the group velocity can be derived from the definition in Eq. (73), together with the obtained solutions for the right- and left-handed susceptibilities in Eqs. (121a)-(121b). Following the definition of the detunings in Eqs. (98a)-(98c), the derivative term in Eq. (73) can be transformed as follows:

$$\frac{\partial}{\partial\omega} \to -\frac{\partial}{\partial\Delta}, \tag{129}$$

such that we have:

$$\frac{\partial\chi_k}{\partial\omega} = 2\zeta c\Gamma\sigma_k \left[\frac{D'}{\omega D^2} - \frac{1}{\omega^2 D}\right], \tag{130}$$

where $k = R, L$, while σ_k, D and D' are defined as:

$$\sigma_R = \cos^2\theta + \frac{\Omega_R}{\Omega_L}\sin\theta\cos\theta, \tag{131a}$$

$$\sigma_L = \frac{\Omega_L}{\Omega_R}\sin\theta\cos\theta + \sin^2\theta, \tag{131b}$$

$$D = \Delta - \frac{|\Omega_C|^2}{\Delta - \Delta_3 + 2i\gamma_d} + i(\Gamma + \gamma_d). \tag{131c}$$

$$D' = \frac{\mathrm{d}D}{\mathrm{d}\Delta} = 1 + \frac{|\Omega_C|^2}{(\Delta - \Delta_3 + 2i\gamma_d)^2} \tag{131d}$$

The second term inside the brackets on the right-hand side of Eq. (130) can typically be neglected because the optical frequency ω is very large, such that the $1/\omega^2$ term decays rapidly compared with the $1/\omega$ term. Under this approximation, Eq. (130) reduces to:

$$\frac{\partial\chi_k}{\partial\omega} \approx \frac{2\zeta c\Gamma\sigma_k}{\omega}\frac{D'}{D^2}. \tag{132}$$

Therefore, by substituting Eq. (132) into Eq. (73), we can obtain the following expression for the group velocity of the right- and left-handed beam components:

$$v_{g,k} \approx \frac{c}{1 + c\zeta\Gamma\mathrm{Re}\left[\sigma_\mathrm{k}\frac{\mathrm{D}'}{\mathrm{D}^2}\right]}, \quad k = R, L. \tag{133}$$

To provide an example of the group velocity behavior in a well-characterized atomic medium, we consider for instance, a cold ^{87}Rb atomic system in which the vector vortex optical frequency is close to the D2 hyperfine transition of the atom. An experimental scheme for the interaction of a vector vortex beam with this atomic system can be based on the setup used in [21]. The ^{87}Rb atoms are trapped in a spontaneous-force optical trap (SPOT) [53], where an atomic density of $N = 2 \times 10^{11}$ cm^{-3} is achievable in the experiment [21]. The optical frequency of the D2 transition line in ^{87}Rb is $\omega = 2\pi \times 384$ THz, with a radiative decay rate of $\gamma = 2\pi \times 6$ MHz. Using the definition of ζ and the relation $\Gamma = \frac{3}{2}\gamma$, which follows from the assumption that the decay rates from the excited state to each ground state are equal, we calculate $c\zeta\Gamma = 1.67 \times 10^{20}$ s^{-2}. From this, we obtain the plot of group velocity variation with respect to the normalized detuning Δ/Γ, as illustrated in Fig. 13. The plots are calculated at $z = 0$ and at a fixed radial position, $r = w$, for specific azimuthal angles $\phi = 0, \pi/4$ and $3\pi/8$. The other parameters are the same as those in Fig. 12. It can be seen that, for both the right- and left-handed components, the group velocities are dramatically reduced by almost four orders of magnitude compared with the speed of light in vacuum because of the presence of the control field in a very narrow detuning region close to the two-photon resonance.

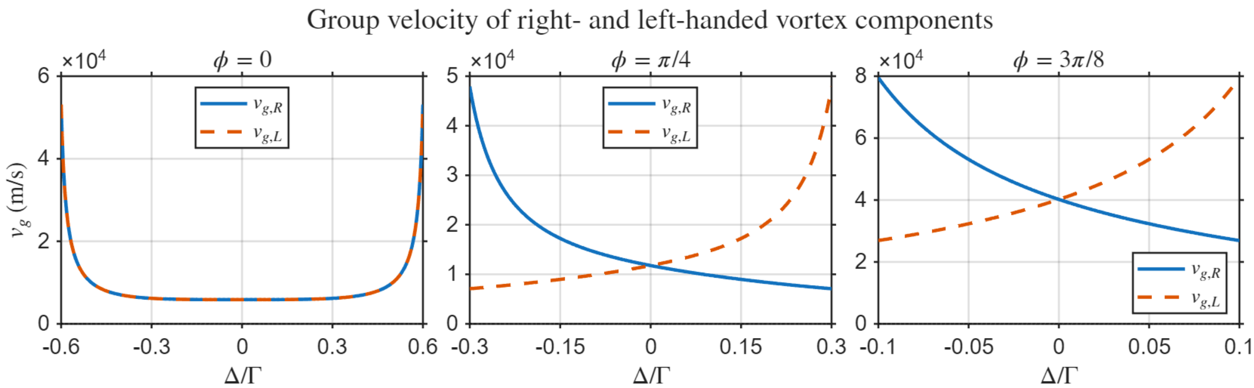

Figure 13: Variation of the group velocity in m/s against normalized detuning Δ/Γ. The parameters used are $\gamma_d = 10^{-3}\Gamma$, $|\Omega_C| = \Gamma$, $\theta = \pi/4$, $\alpha = \pi/4$, and $\varphi = 0$. The plots are calculated at $z = 0$, with $r = w$, for $\phi = 0, \pi/4, 3\pi/8$. The blue lines correspond to the group velocity of the right-handed component, while the red-dashed lines correspond to the left-handed component.

3.1.3 Intensity evolution

The evolution of the absorption profiles of the right- and left-handed components along with the corresponding total intensity distribution in the transverse plane for the beam with $|l| = 1$ are illustrated in Fig. 14(a) where the control field is present with fixed magnitude $|\Omega_C| = \Gamma$, and Fig. 14(b) where the control field is absent. The system is under two-photon resonance $\Delta/\Gamma = 0$, and the propagation distances used are in the normalized form ζz, allowing the behavior to be generalized for any atomic media, as ζ contains the atomic parameters. The first and second rows shows the absorption patterns of the right- and left-handed components, respectively, while the third row shows the evolution of the total intensity. For $|l| = 1$, two azimuthal transparency windows depicted as dark regions are formed, corresponding to $\mathrm{Im}[\chi^{(1)}_{R(L)}] = 0$. At the same time, two complementary regions of non-zero absorption (bright regions) are present. However, the non-zero absorption regions in the presence of the control field have lower magnitude compared to the case without the control field. Nevertheless, the absorption patterns indicate that the $2|l|$-fold degeneracy in the Λ configuration without the control field, as discussed in our previous work [25], remains preserved

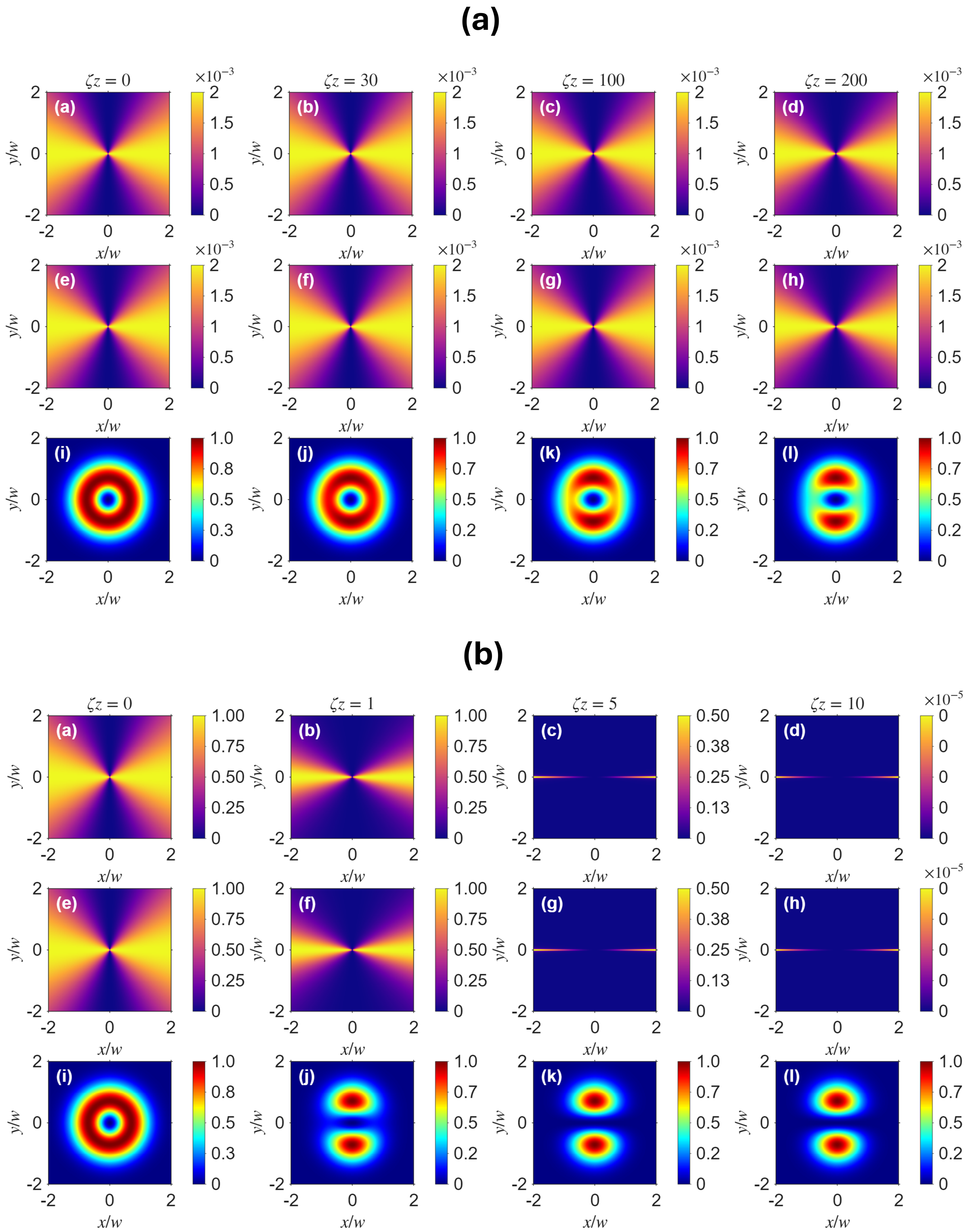

Figure 14: Evolution of the transverse absorption profiles of the right- and left-handed components, together with the total intensity distribution, at different normalized propagation distances ζz for $|l| = 1$ at the two-photon resonance $\Delta/\Gamma = 0$. The first row shows the absorption of the right-handed component, the second row shows the absorption of the left-handed component, and the third row shows the combined total intensity of both components. All other parameters beside the control field are the same as in Fig. 12. (a) $|\Omega_C| = \Gamma$. (b) $|\Omega_C| = 0$.

in the presence of the control field, although with a suppressed absorption. The suppressed absorption affects the evolution rate of the beam intensity, such that the transformation of the intensity profile from a ring-shaped into a petal-like structure requires longer propagation distance. It can be seen by comparing the intensity evolution in the third rows of Figs. 14(a) and 14(b). In the absence of the control field, the petal-like structure is already formed after a short propagation distance, at $\zeta z = 1$, whereas in the presence of the control field, the ring-shaped intensity remains preserved up to $\zeta z = 30$.

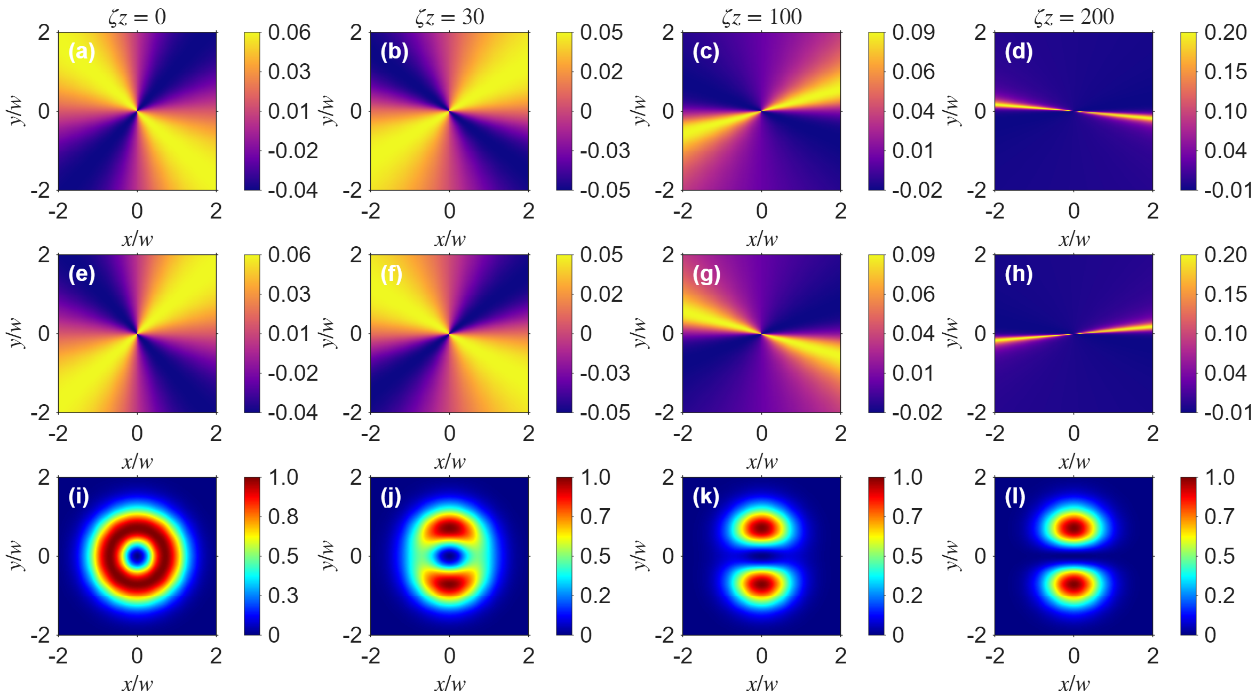

Figure 15: Evolution of the transverse absorption profiles of the right- and left-handed components, together with the total intensity distribution, at different normalized propagation distances ζz for $|l| = 1$ at small detuning from resonance $\Delta = 0.1\Gamma$. The first row shows the absorption of the right-handed component, the second row shows the absorption of the left-handed component, and the third row shows the combined total intensity of both components. All other parameters are the same as in Fig. 12

Figure 15 shows the evolution of the absorption patterns for both circularly polarized components and the corresponding total intensity in a slightly detuned regime, $\Delta = 0.1\Gamma$. The other parameters are the same as those in Fig. 14(a). In this regime, the right- and left-handed components exhibit spatial patterns of amplification and absorption that are complementary to each other. For the right-handed component shown in the first row, two amplification windows appear for $|l| = 1$, shown as dark regions that correspond to $\mathrm{Im}[\chi_R^{(1)}] < 0$. These amplification regions spatially coincide with the absorption windows of the left-handed component, shown in the second row, where $\mathrm{Im}[\chi_L^{(1)}] > 0$, and vice versa. This complementary gain–loss behavior originates from the $\pm i \tan(l\phi)$ term in the susceptibilities in Eqs. (128a)-(128b). The right-handed susceptibility contains $+i \tan(l\phi)$ term, whereas the left-handed susceptibility contains $-i \tan(l\phi)$ term, leading to a generation of spatially dependent gain and loss for non-zero OAM charge l, with opposite rotational symmetries for the two polarization components. The total intensity of the beam still follows the evolution from a ring-shaped structure into a petal-like structure, since the dynamics of the total intensity contains the combination of the overall absorption structure of the whole cross section simultaneously. However, each polarization component experiences a dynamics in the propagation, during which the gain and loss regions rotate and vary in size. This evolving spatial imbalance gives rise to a continuously changing local polarization state, which will be examined in the next section.

3.2 Polarization dynamics of the optical vector vortices in the tripod atomic configuration

To analyze the polarization evolution of slow-light vector vortices as they propagate inside the tripod atomic medium, we rewrite Eqs. (117a)-(117c) in terms of the electric-field amplitudes instead of Rabi frequencies. The polarization states are then computed using the Stokes parameters in the circular polarization basis given in Eqs. (126a)-(126d). The relation between the Rabi frequencies and the corresponding electric-field amplitudes is given by $\Omega_{R(L)} = \vec{d} \cdot \vec{E}_{R(L)}/\hbar$. Assuming equal dipole moments for the right- and left-handed transitions ($d_R = d_L = d$), the field amplitudes can be written as

$$\begin{aligned} E_R(z) =& \tilde{\varepsilon} \sin{(\alpha)} e^{i\varphi} A(r) e^{il\phi} \left(\sin^2{(\theta)} + \cos^2{(\theta)} e^{-i\zeta z} \right) \\ &+ \tilde{\varepsilon} \cos{(\alpha)} A(r) e^{-il\phi} \sin{(\theta)} \cos{(\theta)} \left(e^{-i\zeta z} - 1 \right), \end{aligned} \tag{134a}$$

$$\begin{aligned} E_L(z) =& \tilde{\varepsilon} \sin{(\alpha)} e^{i\varphi} A(r) e^{il\phi} \sin{(\theta)} \cos{(\theta)} \left(e^{-i\zeta z} - 1 \right) \\ &+ \tilde{\varepsilon} \cos{(\alpha)} A(r) e^{-il\phi} \left(\cos^2{(\theta)} + \sin^2{(\theta)} e^{-i\zeta z} \right), \end{aligned} \tag{134b}$$

where $A(r)$ is defined in Eq. (93), and $\tilde{\varepsilon}$ is a scaling factor related to the Rabi amplitude ε through $\tilde{\varepsilon} = \hbar\varepsilon/d$. The total electric field at an arbitrary propagation distance z is expressed as the superposition of its circular polarization components, $\vec{E}(r, \phi, z) = E_R(z)\vec{e}_R + E_L(z)\vec{e}_L$. By tuning the parameters α and θ, the input polarization structure and the initial atomic population distribution can be independently controlled, shaping the following polarization evolution.

3.2.1 Resonant case

We first examine the resonant case, $\Delta = 0$, with the input-beam amplitude tuning angle chosen as $\alpha = \pi/8$. Under this condition, the initial polarization is dominated by the left-handed circular component. The control field is applied with strength $|\Omega_C| = \Gamma$, enabling slow-light propagation of the vector vortex beam. Figure 16(a) shows the case where the atomic population is fixed at $\theta = \pi/4$, corresponding to equal initial populations in the two ground states $|1\rangle$ and $|2\rangle$ before their interaction with the vortex components and the control field. At the entrance of the medium, $\zeta z = 0$, three different polarization textures appear depending on the relative phase φ: radial for $\varphi = 0$, spiral for $\varphi = \pi/2$, and azimuthal for $\varphi = \pi$. In all cases, the intensity exhibits a ring-shaped profile corresponding to the topological charge $|l| = 1$. As the beam propagates through the medium, the intensity distribution slowly transforms from a ring into a petal-like structure with two lobes, where the orientation is determined by the relative phase φ. Remarkably, after the petal pattern is fully established and the system approaches a quasi-stationary regime, the polarization texture transforms from the initial left-handed circular polarization, indicated by red ellipses, into linear polarization states, represented by yellow lines. This transformation occurs for all values of

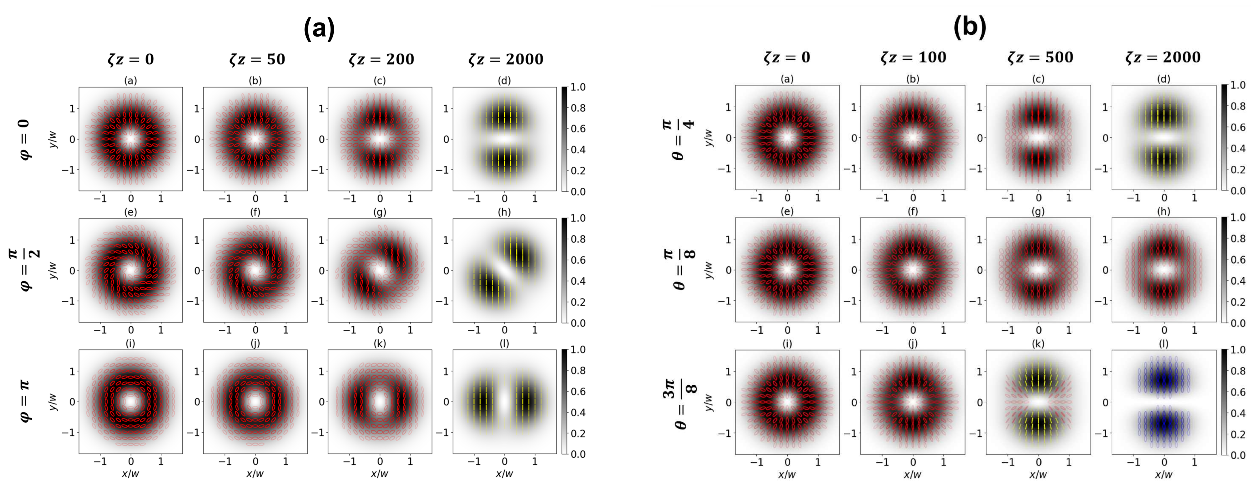

Figure 16: Intensity profile and polarization state evolution in the transverse plane of the vector vortex with $|l| = 1$ and relative amplitude $\alpha = \pi/8$, such that the initial polarization state at the medium entrance is dominated by the left-handed circular polarization ($|E_L(0)| > |E_R(0)|$). The transverse coordinates (x, y) are normalized to the beam waist w, with the propagation distance expressed as the dimensionless parameter ζz. The vector vortex beam is in two-photon resonance with detuning $\Delta = 0$, while the other parameters are $\gamma_d = 10^{-3}\Gamma$ and $|\Omega_C| = \Gamma$. Darker rings or lobes correspond to higher intensity regions. The red and blue ellipses denote the the left- and right-circular polarization states, respectlively, while yellow lines indicate the linear polarization state. (a) The initial phaseonium state is fixed at $\theta = \pi/4$; the first, second, and third rows correspond to relative phases $\varphi = 0, \pi/2, \pi$, respectively. (b) The relative phase is fixed at $\varphi = 0$; the first, second, and third rows correspond to initial phaseonium state $\theta = \pi, \pi/4, 3\pi/8$, respectively.

φ, indicating that the transition from circular to linear polarization is largely independent of the initial relative phase.

In Figure 16(b), we set $\varphi = 0$ and vary the initial atomic population through the tuning angle θ. The first row shows the case $\theta = \pi/4$, corresponding to equal initial populations in the ground states $|1\rangle$ and $|2\rangle$. The second row represents $\theta = \pi/8$, for which $|1\rangle$ is initially more populated than $|2\rangle$, while the third row corresponds to $\theta = 3\pi/8$, where $|1\rangle$ is initially less populated than $|2\rangle$. During propagation of the slow-light vector vortex, the intensity distribution gradually changes from a ring-shaped profile into a petal-like structure. Because the relative phase φ is fixed, the lobes do not rotate in any of the cases. Interestingly, the stationary polarization state reached at the end of propagation is determined only by the initial population imbalance. For $\theta = \pi/4$, the beam approaches a linearly polarized state, indicated by the yellow lines. For $\theta = \pi/8$, it maintains left-handed circular polarization, shown by the red ellipses. In contrast, for $\theta = 3\pi/8$, it evolves toward right-handed circular polarization, represented by the blue ellipses, at sufficiently large propagation distances. These results show that the final polarization texture of slow-light vector vortices can be controlled directly by tuning the initial atomic population superposition.

3.2.2 Small detuned case

Next, in Figure 17(a), we consider a slightly detuned case by setting $\Delta = 0.1\Gamma$, while keeping the control-field strength $|\Omega_C|$ and all other parameters identical to those used in Fig. 16(b). In this near-resonant regime, perfect EIT is no longer achieved, and the strong absorption suppression observed at $\Delta = 0$ is slightly weakened. Even so, the absorption remains minimal and the dispersion retains a positive slope, as shown in the subplot of Fig. 12, allowing effective slow-light propagation of the vector vortex beam.

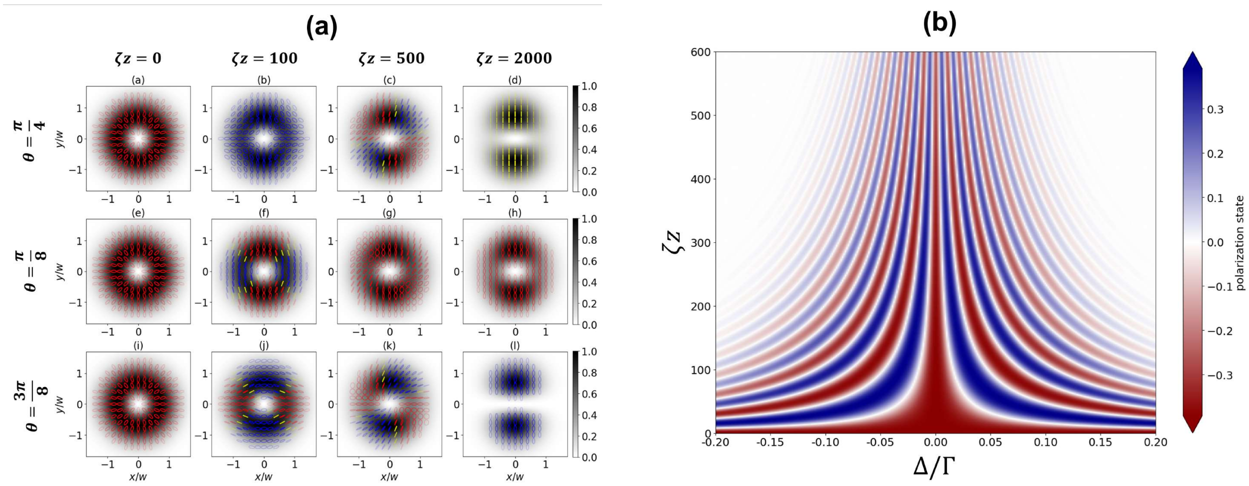

Figure 17: Intensity profile and polarization state evolution (a), and ellipticity distribution (b) of the vector vortex with $|l| = 1$ and relative amplitude $\alpha = \pi/8$, such that the initial polarization state at the medium entrance is dominated by the left-handed circular polarization ($|E_L(0)| > |E_R(0)|$). The propagation distance is expressed as the dimensionless parameter ζz. The relative phase is fixed at $\varphi = 0$, while the other parameters are $\gamma_d = 10^{-3}\Gamma$ and $|\Omega_C| = \Gamma$. (a) The detuning is fixed at $\Delta = 0.1\Gamma$; the first, second, and third rows correspond to initial phaseonium states $\theta = \pi/4, \pi/8, 3\pi/8$, respectively. Darker rings or lobes correspond to higher intensity regions. The red and blue ellipses denote the left- and right-handed circular polarization states, respectively, while yellow lines indicate linear polarization states. (b) The initial phaseonium state is fixed at $\theta = \pi/4$; the plot shows the average ellipticity corresponding to linear, left- and right-handed circular polarization states, denoted by white, dark red, and dark blue colors, respectively, at different propagation distances ζz and detuning values Δ/Γ.

The introduction of a small detuning produces oscillatory polarization dynamics at intermediate propagation distances before the system reaches its stationary state. At this stage, the intensity distribution has not yet fully developed into a lobe structure, as seen at $\zeta z = 100$ and $\zeta z = 500$. These oscillations originate from the spatially dependent and complementary gain-loss behavior of the right- and left-handed components, discussed in Fig. 15(b). As the beam continues to propagate, the gain-loss regions evolve dynamically, rotating in opposite directions for the two components while also changing in size. This evolution drives continuous variations of the local polarization state across the transverse plane, with the polarization cycling among left-handed circular, linear, and right-handed circular states at different azimuthal positions. Importantly, complete conversion from left- to right-handed circular polarization can occur at intermediate propagation distances while the ring-shaped intensity profile is still largely maintained, as observed for $\theta = \pi/4$ at $\zeta z = 100$. A similar conversion also appears at very large propagation distances, $\zeta z = 2000$, for $\theta = 3\pi/8$, after the intensity has evolved into a lobe pattern. This behavior shows that slow-light vector vortices can preserve rich and robust polarization dynamics even when the system is slightly detuned from resonance.

To demonstrate the continuous and periodic evolution of the polarization states before the system enters a stationary regime, we calculate the average ellipticity over the non-zero-intensity region of the beam cross section for different normalized propagation distances ζz and detunings Δ/Γ. The results are presented in Fig. 17(b) for $\theta = \pi/4$, where left- and right-handed circular polarizations are represented by red and blue, respectively, while linear polarization is shown in white to clearly distinguish the three polarization states. From $\zeta z = 0$ to $\zeta z = 600$, the polarization undergoes periodic transitions from left-handed circular polarization to linear polarization and then to right-handed circular polarization for nonzero detuning, $\Delta/\Gamma \neq 0$. At larger propagation distances, the system eventually reaches a stationary regime, where the polarization remains linear as a consequence of the chosen atomic population parameter $\theta = \pi/4$. The colormap further indicates that increasing the detuning from resonance reduces the propagation distance needed to reach this stationary state. This behavior is associated with stronger medium losses, which accelerate the transformation of the ring-shaped intensity profile into a lobe structure. The response is also symmetric for positive and negative detunings.

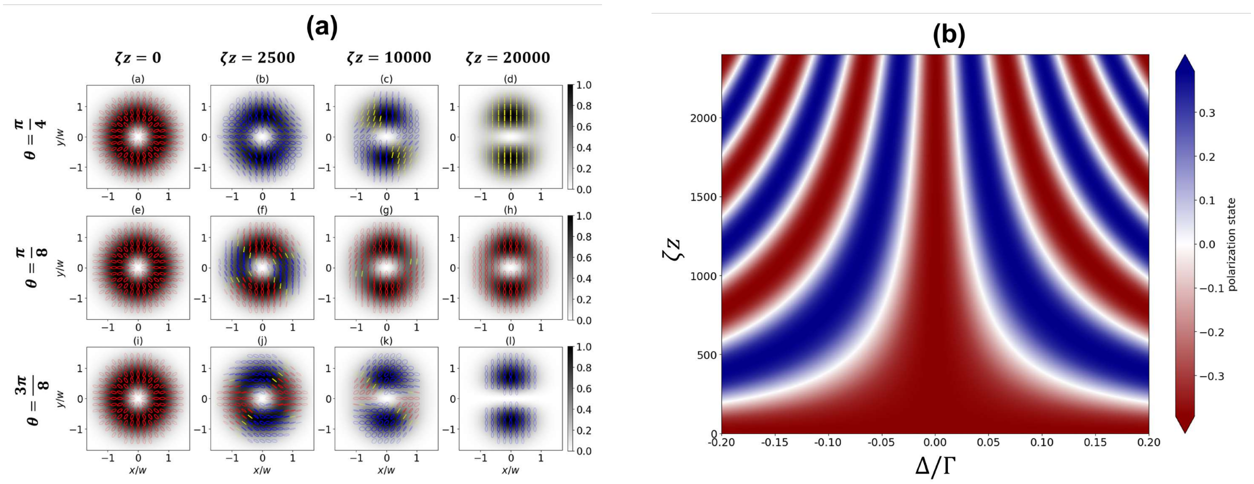

Figure 18: Intensity profile and polarization state evolution (a), and ellipticity distribution (b) of the vector vortex with $|l| = 1$ and relative amplitude $\alpha = \pi/8$, such that the initial polarization state at the medium entrance is dominated by the left handed circular polarization ($|E_L(0)| > |E_R(0)|$). The propagation distance is expressed as the dimensionless parameter ζz. The relative phase is fixed at $\varphi = 0$ while the other parameters are $\gamma_d = 10^{-3}\Gamma$ and $|\Omega_C| = 5\Gamma$. (a) The detuning is fixed at $\Delta = 0.1\Gamma$; the first, second, and third rows correspond to initial phaseonium states $\theta = \pi/4, \pi/8, 3\pi/8$, respectively. Darker rings or lobes correspond to higher intensity regions. The red and blue ellipses denote the left- and right-handed circular polarization states, respectively, while yellow lines indicate linear polarization states. (b) The initial phaseonium state is fixed at $\theta = \pi/4$; the plot shows the average ellipticity corresponding to linear, left- and right-handed circular polarization states, denoted by white, dark red, and dark blue colors, respectively, at different propagation distances ζz and detuning values Δ/Γ.

In Figure 18(a), we consider a stronger control field, $|\Omega_C| = 5\Gamma$, while keeping all other parameters identical to those used in Fig. 17(a). The increased control-field strength substantially suppresses the overall absorption in the system, thereby slowing the evolution of both the beam intensity distribution and the associated polarization states. Consequently, the propagation distance required for the system to reach its stationary regime increases by approximately one order of magnitude compared with the small-detuning case under the weaker control field shown in Fig. 17(a). Figure 18(b) shows the average ellipticity across the non-zero-intensity region of the beam cross section as a function of the normalized propagation distance ζz and detuning Δ/Γ, for the atomic population parameter $\theta = \pi/4$. For nonzero detuning, the beam maintains nearly constant circular polarization over a longer propagation distance before undergoing periodic transitions into linear and opposite circular polarization states. This is in contrast to the more rapid polarization oscillations observed for the weaker control field in Fig. 17(b). This behavior may be experimentally beneficial, since the medium length can be selected such that polarization flipping occurs at an intermediate propagation distance where the ring-shaped intensity profile remains largely preserved, allowing the information encoded in the beam intensity to be maintained.

4 Conclusion

1. Spatially dependent absorption, dispersion, and optical spin-orbit coupling have been demonstrated in a coherently prepared four-level tripod configuration interacting with a vector vortex beam carrying opposite vorticities $\pm l$ and circular polarization states of opposite handedness, together with a strong control field without orbital angular momentum.

2. It has been numerically demonstrated that $2|l|$-fold degenerate transparency windows are formed under the resonant condition $\Delta/\Gamma = 0$, while $2|l|$-fold complementary absorption and weak-gain regions are formed in the slightly detuned region $\Delta/\Gamma \neq 0$ for equal ground-state populations, $\theta = \pi/4$. The transparency windows under the resonant condition, and the complementary absorption-gain windows correspond to the formation of a petal-like pattern as the beam propagates deeper inside the medium.

3. The presence of the control field affects the order of magnitude of the transparency windows under the resonant condition, and the complementary absorption-gain windows, while preserving the azimuthally dependent spatial structure. As a result, the intensity transformation occurs more gradually, requiring larger propagation distances.

4. The presence of the control field also affects the dispersion behavior, where a dramatic reduction in the group-velocity is demonstrated in the slightly detuned region very close to the resonance, $\Delta \leq 0.1\Gamma$.

5. A SAM exchange that corresponds to a polarization-state transition was observed in the presence of the strong control field. This exchange was shown to depend on the initial ground-state populations and the detuning, regardless of the initial polarization state and relative phase φ at $z = 0$.

6. The strength of the control field is shown to affect the polarization-state evolution, where a stronger control field leads to a slower evolution rate.

References

[1] P. Coullet, L. Gil, and F. Rocca, Optical vortices, *Optics Communications*, 1989, **73**, 403–408.

[2] G. Gibson, J. Courtial, M. J. Padgett, M. Vasnetsov, V. Pas'ko, S. M. Barnett, and S. Franke-Arnold, Free-space information transfer using light beams carrying orbital angular momentum, *Opt. Express*, Nov 2004, **12**, 5448–5456.

[3] S. R. Park, L. Cattell, J. M. Nichols, A. Watnik, T. Doster, and G. K. Rohde, De-multiplexing vortex modes in optical communications using transport-based pattern recognition, *Opt. Express*, Feb 2018, **26**, 4004–4022.

[4] M. Erhard, R. Fickler, M. Krenn, and A. Zeilinger, Twisted photons: new quantum perspectives in high dimensions, *Light: Science & Applications*, Mar 2018, **7**, 17146–17146.

[5] S. Z. D. Plachta, M. Hiekkamäki, A. Yakaryılmaz, and R. Fickler, Quantum advantage using high-dimensional twisted photons as quantum finite automata, *Quantum*, June 2022, **6**, 752.

[6] L. Allen, M. W. Beijersbergen, R. J. C. Spreeuw, and J. P. Woerdman, Orbital angular momentum of light and the transformation of laguerre-gaussian laser modes, *Phys. Rev. A*, Jun 1992, **45**, 8185–8189.

[7] M. Brambilla, F. Battipede, L. A. Lugiato, V. Penna, F. Prati, C. Tamm, and C. O. Weiss, Transverse laser patterns. i. phase singularity crystals, *Phys. Rev. A*, May 1991, **43**, 5090–5113.

[8] P. Zhang, B.-H. Liu, R.-F. Liu, H.-R. Li, F.-L. Li, and G.-C. Guo, Implementation of one-dimensional quantum walks on spin-orbital angular momentum space of photons, *Phys. Rev. A*, May 2010, **81**, 052322.

[9] K.-J. Boller, A. Imamoğlu, and S. E. Harris, Observation of electromagnetically induced transparency, *Phys. Rev. Lett.*, May 1991, **66**, 2593–2596.

[10] M. Fleischhauer and M. D. Lukin, Dark-state polaritons in electromagnetically induced transparency, *Phys. Rev. Lett.*, May 2000, **84**, 5094–5097.

[11] M. Fleischhauer, A. Imamoglu, and J. P. Marangos, Electromagnetically induced transparency: Optics in coherent media, *Rev. Mod. Phys.*, Jul 2005, **77**, 633–673.

[12] J. Ruseckas, V. c. v. Kudriašov, I. A. Yu, and G. Juzeliūnas, Transfer of orbital angular momentum of light using two-component slow light, *Phys. Rev. A*, May 2013, **87**, 053840.

[13] H. R. Hamedi, J. Ruseckas, E. Paspalakis, and G. Juzeliūnas, Transfer of optical vortices in coherently prepared media, *Phys. Rev. A*, Mar 2019, **99**, 033812.

[14] H. R. Hamedi, V. Kudriašov, J. Ruseckas, and G. Juzeliūnas, Azimuthal modulation of electromagnetically induced transparency using structured light, *Opt. Express*, Oct 2018, **26**, 28249–28262.

[15] Q.-F. Chen, B.-S. Shi, Y.-S. Zhang, and G.-C. Guo, Entanglement of the orbital angular momentum states of the photon pairs generated in a hot atomic ensemble, *Phys. Rev. A*, Nov 2008, **78**, 053810.

[16] C. Rosales-Guzmán, B. Ndagano, and A. Forbes, A review of complex vector light fields and their applications, *Journal of Optics*, Nov 2018, **20**, 123001.

[17] A. M. Yao and M. J. Padgett, Orbital angular momentum: origins, behavior and applications, *Adv. Opt. Photon.*, Jun 2011, **3**, 161–204.

[18] C. J. Gibson, P. Bevington, G.-L. Oppo, and A. M. Yao, Control of polarization rotation in nonlinear propagation of fully structured light, *Phys. Rev. A*, Mar 2018, **97**, 033832.

[19] N. Daloi and T. N. Dey, Vector beam polarization rotation control using resonant magneto optics, *Opt. Express*, Jun 2022, **30**, 21894–21905.

[20] Y. Ma, X. Yang, H. Chang, M.-T. Cao, X.-F. Zhang, R.-F. Dong, and S.-G. Zhang, Modulation of bessel-like vector vortex beam using the resonant magneto-optical effect in rubidium vapor, *Chinese Physics B*, jan 2025, **34**, 024202.

[21] N. Radwell, T. W. Clark, B. Piccirillo, S. M. Barnett, and S. Franke-Arnold, Spatially dependent electromagnetically induced transparency, *Phys. Rev. Lett.*, Mar 2015, **114**, 123603.

[22] S. Sharma and T. N. Dey, Phase-induced transparency-mediated structured-beam generation in a closed-loop tripod configuration, *Phys. Rev. A*, Sep 2017, **96**, 033811.

[23] F. Castellucci, T. W. Clark, A. Selyem, J. Wang, and S. Franke-Arnold, Atomic compass: Detecting 3d magnetic field alignment with vector vortex light, *Phys. Rev. Lett.*, Nov 2021, **127**, 233202.

[24] V. Kudriašov, M. M. Sinkevičienė, N. Daloi, J. Ruseckas, T. N. Dey, S. Franke-Arnold, and H. R. Hamedi, Propagation of optical vector and scalar vortices in an atomic medium with closed-loop tripod configuration, *Opt. Express*, Sep 2025, **33**, 40931–40947.

[25] D. P. Permana, M. M. Sinkevičienė, J. Ruseckas, and H. R. Hamedi, Spin-orbit coupling of optical vector vortices in coherently prepared media, *Phys. Rev. A*, Apr 2026, **113**, 043705.

[26] L. V. Hau, S. E. Harris, Z. Dutton, and C. H. Behroozi, Light speed reduction to 17 metres per second in an ultracold atomic gas, *Nature*, Feb 1999, **397**, 594–598.

[27] E. Paspalakis and P. L. Knight, Electromagnetically induced transparency and controlled group velocity in a multilevel system, *Phys. Rev. A*, Jul 2002, **66**, 015802.

[28] G. Juzeliūnas and P. Öhberg, Slow light in degenerate fermi gases, *Phys. Rev. Lett.*, Jul 2004, **93**, 033602.

[29] H. Wang, D. Goorskey, and M. Xiao, Enhanced kerr nonlinearity via atomic coherence in a three-level atomic system, *Phys. Rev. Lett.*, Jul 2001, **87**, 073601.

[30] Y. Niu and S. Gong, Enhancing kerr nonlinearity via spontaneously generated coherence, *Phys. Rev. A*, May 2006, **73**, 053811.

[31] H. R. Hamedi and G. Juzeliūnas, Phase-sensitive kerr nonlinearity for closed-loop quantum systems, *Phys. Rev. A*, May 2015, **91**, 053823.

[32] D. F. Phillips, A. Fleischhauer, A. Mair, R. L. Walsworth, and M. D. Lukin, Storage of light in atomic vapor, *Phys. Rev. Lett.*, Jan 2001, **86**, 783–786.

[33] J. Otterbach, J. Ruseckas, R. G. Unanyan, G. Juzeliūnas, and M. Fleischhauer, Effective magnetic fields for stationary light, *Phys. Rev. Lett.*, Jan 2010, **104**, 033903.

[34] T. Peters, Y.-H. Chen, J.-S. Wang, Y.-W. Lin, and I. A. Yu, Observation of phase variation within stationary light pulses inside a cold atomic medium, *Opt. Lett.*, Jan 2010, **35**, 151–153.

[35] U.-S. Kim and Y.-H. Kim, Simultaneous trapping of two optical pulses in an atomic ensemble as stationary light pulses, *Phys. Rev. Lett.*, Aug 2022, **129**, 093601.

[36] M. O. Scully and M. S. Zubairy, *Quantum Optics*. Cambridge University Press, 1997.

[37] R. Finkelstein, S. Bali, O. Firstenberg, and I. Novikova, A practical guide to electromagnetically induced transparency in atomic vapor, *New Journal of Physics*, mar 2023, **25**, 035001.

[38] M. Fleischhauer and G. Juzeliūnas, *Slow, Stored and Stationary Light*, 359–383. Cham: Springer International Publishing, 2016.

[39] S. E. Harris, J. E. Field, and A. Kasapi, Dispersive properties of electromagnetically induced transparency, *Phys. Rev. A*, Jul 1992, **46**, R29(R)–R32(R).

[40] Y. Niu and S. Gong, Enhancing kerr nonlinearity via spontaneously generated coherence, *Phys. Rev. A*, May 2006, **73**, 053811.

[41] S. Fu and C. Gao, *Optical Vortex Beams: Fundamentals and Techniques*. Springer Nature Singapore, 2023.

[42] S. Ngcobo, I. Litvin, L. Burger, and A. Forbes, A digital laser for on-demand laser modes, *Nature Communications*, Aug. 2013, **4**.

[43] Q. Zhan, Cylindrical vector beams: from mathematical concepts to applications, *Adv. Opt. Photon.*, Jan 2009, **1**, 1–57.

[44] D. G. Hall, Vector-beam solutions of maxwell's wave equation, *Opt. Lett.*, Jan 1996, **21**, 9–11.

[45] A. A. Tovar, Production and propagation of cylindrically polarized laguerre–gaussian laser beams, *J. Opt. Soc. Am. A*, Oct 1998, **15**, 2705–2711.

[46] L. Novotny and B. Hecht, *Principles of Nano-Optics*. Cambridge University Press, June 2006.

[47] A. M. Beckley, T. G. Brown, and M. A. Alonso, Full poincaré beams, *Opt. Express*, May 2010, **18**, 10777–10785.

[48] J. Wang, S. J. Svensson, T. W. Clark, *et al.*, Measuring the optical concurrence of vector beams with an atomic-state interferometer, *Phys. Rev. Lett.*, May 2024, **132**, 193803.

[49] N. V. Vitanov, A. A. Rangelov, B. W. Shore, and K. Bergmann, Stimulated raman adiabatic passage in physics, chemistry, and beyond, *Rev. Mod. Phys.*, Mar 2017, **89**, 015006.

[50] B. Henderson and G. F. Imbusch, *Optical spectroscopy of inorganic solids*. Monographs on the physics and chemistry of materials ; 44, Oxford: Clarendon Press, 2023.

[51] M. Born, E. Wolf, A. B. Bhatia, *et al.*, *Principles of Optics: Electromagnetic Theory of Propagation, Interference and Diffraction of Light*. Cambridge University Press, 7 ed., 1999.

[52] S. Rebić, D. Vitali, C. Ottaviani, P. Tombesi, M. Artoni, F. Cataliotti, and R. Corbalán, Polarization phase gate with a tripod atomic system, *Phys. Rev. A*, Sep 2004, **70**, 032317.

[53] N. Radwell, G. Walker, and S. Franke-Arnold, Cold-atom densities of more than 10^{12} cm^{-3} in a holographically shaped dark spontaneous-force optical trap, *Phys. Rev. A*, Oct 2013, **88**, 043409.

Acknowledgement

Firstly, I would like to thank Dr. Hamid Reza Hamedi and Dr. Mažena Mackoit Sinkevičienė, my supervisors, for the opportunity that was given to me. I remember the first time I sent my application to become their master's thesis student; I had very minimal experience working on topics related to quantum mechanics. My initial goal was only to study and try to "taste" what quantum mechanics is really like at the research level, as I thought back then that this master's thesis might be the last chance for me to try it before devoting my life to a specific niche of research direction for my Ph.D. Yet, they still trusted me to work with them and gave me tremendous support along the way. I never imagined that, in less than a year, we would manage to publish two papers together and present our results at multiple conferences. But the most important thing is that I learned a lot during this journey and finally found the niche that I am going to explore for many years from now in my life. Even though I will leave Lithuania and start a new journey as a Ph.D. student in another part of the world, I hope that we can still collaborate and work together to explore more exciting and curious ideas in the future.

Secondly, I would like to express my gratitude to the Cold Atoms and Condensed Molecular Structures Group, in particular Prof. Gediminas Juzeliūnas, Dr. Viačeslav Kudriašov, Dr. Viktor Novičenko, Ph.D. student Dominykas Borodinas, and Ph.D. student Domantas Burba, for all the fruitful discussions, valuable input, and shared knowledge during the preparation of this thesis. I also thank Dr. Artūras Acus as the reviewer for my thesis.

I would also like to thank Dr. Julius Ruseckas from the Baltic Institute of Advanced Technologies and Ph.D. student Jorūnas Dobilas from the FTMC. I thank Dr. Julius in particular, as a collaborator and co-author of our papers, for many valuable comments and suggestions throughout the preparation of our papers, and Jorūnas in particular for the valuable help and suggestions for my presentations in the Novian and VITP scholarship competition.

Next, I would like to thank all the people in the Laser Research Center, in particular Dr. Viktorija Tamulienė, for the support given as the coordinator of Europhotonics at Vilnius University. I also thank Prof. Mangirdas Malinauskas, Dr. Julius Vengelis, Ph.D. student Ignas Ignas Lukošiūnas, Dr. Rytis Butkus, and Dr. Mantas Gaidys for all the valuable knowledge they shared in the courses they taught, and also the head of LRC, Dr. Dalia Kaškelytė, for the support given. I also gratefully acknowledge the support of the Erasmus+: Erasmus Mundus programme of the European Union under Convention n^{o} 101128124 — EUROPHOTONICS — ERASMUS-EDU-2023-PEX-EMJMMOB.

Finally, I would like to thank all my family and friends for the support and love given despite the distance between us. To my father and mother, who always trusted me and prayed for me. To my sister, who has always been my source of motivation. To my Europhotonics classmates, who laughed and cried together with me during our journey. Thank you.

Summary

Propagation of Optical Vector Vortices in Coherently Prepared Media

Dharma Prasetya Permana

Decades of intensive investigation on optical vortices has led to growing interest in the utilization of orbital angular momentum (OAM) states of light for quantum communication and quantum information processing [2–5]. To this end, the investigation of optical vortex with a full vectorial consideration interacting with an electromagnetically induced transparency (EIT) media has led to the discovery of spatially dependent transparency [21], and polarization state transitions [24] allowing the manipulation of both the OAM property and the spin angular momentum (SAM) property of light related to its polarization state [8]. These studies has been demonstrated in a system with coherently prepared Λ configuration without a static magnetic field to introduce the quantum coherence [25]. However, these studies of vector vortex beams in the EIT-enabled atomic media has not yet been explored in the context of slow-light propagation regime.

This work aims to investigate the interaction of optical vector vortices with an EIT-enabled atomic medium, where spatially dependent transparency and polarization-state transitions can be realized in the slow-light propagation regime. We consider an alternative configuration based on a coherently prepared four-level tripod atomic scheme, in which a weak vector vortex beam interacts with the medium in the presence of a strong control beam carrying no orbital angular momentum (OAM). The weak vector vortex beam consists of paired vortex pulses carrying opposite OAM charges, $\pm l$, together with opposite spin angular momentum (SAM) associated with orthogonal circular polarizations of opposite handedness. Meanwhile, the control field is taken to have an arbitrary circular polarization but no OAM charge.

In the linear regime, the vortex OAM is mapped onto the atomic medium, giving rise to symmetric azimuthally structured absorption patterns with a strongly suppressed absorption by the control field. For small detunings, complementary spatially dependent amplification and absorption appear for the two circular polarization components. This OAM-structured coherence induces a dynamical anisotropy that influences both the intensity and polarization evolution of the slow-light vortex beam. During propagation, the polarization state evolves periodically among left-handed circular, linear, and right-handed circular polarizations. Once the beam reaches a stationary regime, its ring-shaped intensity profile transforms into a petal-like structure, while the final polarization state stabilizes according to the initial atomic superposition. The rate of these polarization transitions can be tuned through the control-field strength, demonstrating flexible control over slow-light vector vortex dynamics.

Santrauka

Optinių vektorinių sūkurių sklidimas koherentiškai paruoštoje terpėje

Dharma Prasetya Permana

Dešimtmečius trukę intensyvūs optinių sūkurių tyrimai paskatino vis didesnį susidomėjimą šviesos orbitinio kampinio momento (OKM) būsenų panaudojimu kvantinei komunikacijai ir kvantinės informacijos apdorojimui [2–5]. Šiuo tikslu optinių sūkurių tyrimai, apėmę pilną vektorinį sąveikos su elektromagnetiškai indukuoto praskaidrėjimo (EIP) terpe aprašymą, leido atrasti erdviškai priklausomą praskaidrėjimą [21] ir poliarizacijos būsenų perėjimus [24]. Šie reiškiniai sudaro galimybę valdyti tiek orbitinį kampinį momentą (OKM), tiek sukinio kampinį momentą (SKM), susijusį su šviesos poliarizacija [8]. Tačiau iki šiol atlikti tyrimai apsiribojo EIP kilpine–tripodo konfigūracija, kurioje reikalingas silpnas statinis magnetinis laukas kvantinei koherencijai palaikyti. Šie tyrimai buvo pademonstruoti sistemoje su koherentiškai paruošta Λ konfigūracija, kurioje kvantinė koherencija sukuriama nenaudojant statinio magnetinio lauko [25]. Vis dėlto vektorinių sūkurinių pluoštų tyrimai EIT pagrindu veikiančiose atominėse terpėse iki šiol dar nebuvo nagrinėti lėtosios šviesos sklidimo režimo kontekste.

Šiame darbe siekiama ištirti optinių vektorinių sūkurių sąveiką su EIT pagrindu veikiančia atomine terpe, kurioje lėtosios šviesos sklidimo režime gali būti realizuojamas erdviškai priklausomas skaidrumas ir poliarizacijos būsenų perėjimai. Nagrinėjame alternatyvią konfigūraciją, pagrįstą koherentiškai paruošta keturių lygmenų trikojė atominė sistema, kurioje silpnas vektorinis sūkurinis pluoštas sąveikauja su terpe esant stipriam valdymo pluoštui, neturinčiam orbitinio kampinio momento (OKM). Silpnas vektorinis sūkurinis pluoštas sudarytas iš suporuotų sūkurinių impulsų, nešančių priešingus OKM krūvius, $\pm l$, ir priešingą sukininį kampinį momentą (SKM), susijusį su ortogonaliomis apskritiminėmis priešingo sukinio poliarizacijomis. Tuo tarpu valdymo laukas laikomas turinčiu nepriklausomą apskritiminę poliarizaciją, tačiau neturinčiu OKM krūvio.

Tiesiniame režime sūkurio OKM yra perkeliamas į atominę terpę, todėl susidaro simetriški azimutiškai struktūruoti sugerties raštai, kurių sugertis dėl valdymo lauko yra stipriai nuslopinta. Esant mažiems išderinimams, dviem apskritiminės poliarizacijos komponentėms atsiranda viena kitą papildančios erdviškai priklausomos stiprinimo ir sugerties sritys. Ši OKM struktūruota koherencija sukelia dinaminę anizotropiją, darančią įtaką tiek lėtosios šviesos sūkurinio pluošto intensyvumo, tiek poliarizacijos evoliucijai. Sklidimo metu poliarizacijos būsena periodiškai kinta tarp kairinės apskritiminės, tiesinės ir dešininės apskritiminės poliarizacijos. Pluoštui pasiekus stacionarųjį režimą, jo žiedo formos intensyvumo profilis virsta žiedlapio formos struktūra, o galutinė poliarizacijos būsena stabilizuojasi pagal pradinę atominę superpoziciją. Šių poliarizacijos perėjimų spartą galima reguliuoti keičiant valdymo lauko stiprį, taip parodant lankstaus lėtosios šviesos vektorinių sūkurių dinamikos valdymo galimybę.

Approbation of the results

Publications related to the topic of the thesis:

1. **D. P. Permana**, M. M. Sinkevičienė, J. Ruseckas, and H. R. Hamedi, Spin-orbit coupling of optical vector vortices in coherently prepared media, Phys. Rev. A **113**, 043705 (2026)

2. **D. P. Permana**, M. M. Sinkevičienė, J. Ruseckas, and H. R. Hamedi, Propagation of optical vector vortices of slow light in a coherently prepared tripod configuration, Chaos, Solitons, & Fractals **209**, 118518 (2026).

Conference presentations related to the topic of the thesis:

1. **[Oral Presenter] D. P. Permana**, M. M. Sinkevičienė, J. Ruseckas, and H. R. Hamedi, Towards quantum internet with structured lights, "Novian and VITP Named Scholarship Competition", May 14, 2026, Vilnius, Lithuania.

2. **[Oral Presenter] D. P. Permana**, M. M. Sinkevičienė, J. Ruseckas, and H. R. Hamedi, Optical spin-orbit dynamics of vector vortices in coherently prepared media, "69$^{\text{th}}$ International Conference for Students of Physics and Natural Sciences Open Readings 2026", April 27-30, 2026, Vilnius, Lithuania.

3. **[Oral Presenter] D. P. Permana**, M. M. Sinkevičienė, J. Ruseckas, and H. R. Hamedi, Probing coherently prepared atomic systems with structured light beams, "14$^{\text{th}}$ Conference of Young Scientists Interdisciplinary Research in Physical and Technological Sciences", April 17, 2026, Vilnius, Lithuania.

4. **[Poster Presenter] D. P. Permana**, M. M. Sinkevičienė, J. Ruseckas, and H. R. Hamedi, Probing atomic systems with structured light, "15$^{\text{th}}$ EuroPhotonics Spring School 2026", March 23-26, 2026, Barcelona, Spain.

5. **[Oral Presenter] D. P. Permana**, M. M. Sinkevičienė, J. Ruseckas, and H. R. Hamedi, Spin-orbit dynamics of optical vector vortices in coherently prepared atomic media with Λ and tripod configuration, "International Conference on Quantum Photonics Development in Baltic Region", February 11-13, 2026, Riga, Latvia.